Carbon template assisted hydrothermal synthesis of hollow structured nanomaterials and nanocomposites

Md Shahadat Hossain

A dissertation submitted to the graduate faculty in partial fulfilment of the requirements for the degree of

DOCTOR OF PHILOSOPHY

Department: Innovation Systems Engineering

Utsunomiya University

March 2023

Acknowledgements

First and foremost, thanks and praises to the Almighty Allah for His mercy and blessings throughout my research.

I would like to express my deep and sincere gratitude to my research supervisor Professor Dr. Masahide Sato, from the Department of Innovation Systems Engineering, Utsunomiya University, Japan for his constructive advice, inspiring guidance, valuable suggestions, constant encouragement, and support throughout this research work.

I am wholeheartedly thankful to Professor Dr. Takeshi Furusawa, Professor Dr. Noboru Suzuki, Professor Dr. Ken-ichi Iimura, Professor Dr. Toru Oba, Professor Dr. Takafumi Sato, Professor Dr. Keitaro Tezuka, Professor Dr. Taki Matsumoto from Utsunomiya University, Japan and Professor Dr. Newaz Mohammed Bahadur from Noakhali Science and Technology University, Bangladesh for their valuable suggestions, guidance, and support in my research.

I would like to express my special thanks and gratitude to the students from our laboratory who have supported me painstakingly during this research.

The unconditional love, constant support, and cooperation I have received from my family is greatly appreciated.

Finally, I could not end without acknowledging MEXT (Ministry of Education, Culture, Sports, Science and Technology, Government of Japan) and Creative Department for Innovation (CDI), Utsunomiya University, Japan for financial support.

Table of Contents

List of Figures

List of Tables

Abstract

Hollow micro/nanostructures, integrating hollow interiors or voids with mesoporous shells of varying dimensions, are generally characterized by high surface area, faster surface reactions, improved mass transfer, low density, and high permeability. In this study, a simple, cost-effective hydrothermal technique was used to fabricate hollow structured nanomaterials and nanocomposites, using sugar-derived carbon as a hard template. No organic solvent or additive was used. Hollow α-Fe_2O_3 microspheres were synthesized using anhydrous ferric chloride as the precursor and the thermal stability of this material has been demonstrated at high calcination temperatures. ZnO hollow microspheres were successfully prepared using $Zn(NO_3)_2.6H_2O$ as the precursor and its photocatalytic performance was compared with ZnO nanoparticles. ZnO-$ZnFe_2O_4$ hollow composite material with an ultra-high surface area was fabricated using a similar technique. Different characterization techniques such as X-ray diffraction spectroscopy (XRD), field-emission scanning electron microscopy (FE-SEM), energy-dispersive X-ray spectroscopy (EDX), transmission electron microscopy (TEM), X-ray photoelectron spectroscopy (XPS), attenuated total reflectance Fourier-transform infrared spectroscopy (ATR-FTIR), and thermogravimetric analysis coupled with differential thermal analysis (TGA-DTA) were used to analyze the prepared materials. Based on the results, the shell of the hollow structured nanomaterials and nanocomposites was composed of aggregated nanoparticles, while the sugar-derived carbon core was decomposed during calcination, leaving a hollow interior. The diameter of the prepared hollow microspheres was in the range of 500 nm to 2 μm. EDX spectrum of these samples detected the signals of the elements present in these materials, and elemental mapping studies confirmed a homogenous distribution of these elements.

Thermal stability studies of hollow α-Fe_2O_3 microspheres were demonstrated by TGA-DTA analysis, and the data depicted that the material's thermal stability was achieved at 480 °C and no weight loss was observed up to 1000 °C. High-temperature calcination results showed that this material can maintain its hollow morphology up to 700 °C. ZnO hollow microspheres and ZnO nanoparticles of similar crystallite size (around 40 nm) were prepared by hydrothermal and sol-gel techniques, respectively. The photocatalytic efficiency and effectiveness of the hollow morphology of these catalysts for rhodamine blue degradation were studied under ultraviolet light irradiation. The ZnO hollow microspheres showed 10% higher efficiency than ZnO nanoparticles which can be attributed to their nano-porous structure, large surface area, and easy formation of •OH radicals. Hollow microspheres of ZnO-$ZnFe_2O_4$ composite material synthesized by a similar method demonstrated an ultra-high surface area of 1051 m^2g^{-1} which makes this material useful in different surface-related applications. These materials also have potential applications in drug delivery, gas sensing, and lithium storage.

CHAPTER 1

Introduction

The term hollow material refers to materials that have space or cavities inside them or are not solid within [1]. The size of the cavity makes hollow materials extraordinarily advantageous in numerous applications, such as catalysis, photocatalysis, drug delivery, solar cells, supercapacitors, lithium-ion batteries, electromagnetic wave absorption, and sensors, due to their specific surface area, load capacity, material transfer, and storage. Generally, the benefits are mainly reflected in the following aspects:

i. Volume-specific surface area is higher in hollow structures. Thus, the structure can effectively prevent particle accumulation and expose more active sites resulting in greater contact between reactants and active sites [2].
ii. A hollow structure has many pores in its shell. Reactants and products can be transported more rapidly due to the abundance of pores [3,4].
iii. Hollow structures allow for the modulation of product selectivity, thereby increasing yields.
iv. In the shell, numerous and discrete cavities can facilitate the reaction of metastable intermediates at active sites [5,6].
v. Hollow structures have the property of spatial confinement, which allows the reactant molecules to be enriched inside the structure to achieve higher concentrations and accelerate electrode reaction rates [7].
vi. In a hollow structure, the interconnected network can reduce electron transport distances [8].

vii. A hollow structure exhibits a greater degree of structural stability. In numerous studies, it has been demonstrated that this unique structure has better mechanical and chemical stability during catalysis [9].

1.1 Nanotechnology

The term "nanotechnology" refers to the study and control of matter with dimensions of approximately 1–100 nanometers, where unique physical properties enable new applications [10]. Nanotechnology involves manipulating matter on a near-atomic scale to create new devices, materials, and structures. This technology offers scientific advancement in a variety of sectors, including medicine, consumer products, energy, materials, and manufacturing.

1.2 Nanomaterials and nanocomposites

Materials defined as nanomaterials have a size range of roughly 1 to 100 nanometers (nm) or at least one dimension in the nanometer range [11]. The definition of a nanomaterial is never straightforward. For some, the size of the material should be a few nanometers, for others, it should be smaller than a few tens of nanometers, for still others anything less than a micrometer will do. Also, for some, one dimension at the nanoscale is enough; for others, it should be at least two or even all three [12].

The term nanocomposite refers to multiphase materials in which one of the phases has a dimension of less than 100 nanometers; or the phases in the composite have nanoscale distances between them [13].

1.2.1 Hematite (α-Fe_2O_3)

The iron oxide compound hematite, also known as haematite, can be found in rocks and soils and has the formula Fe_2O_3. In ambient conditions, Hematite is more stable than other iron oxide polymorphs and is highly resistant to corrosion. Inversion of maghemite or oxidation of magnetite produces hematite. In addition, it can be formed during oxyexsolution of titanomagnetite when cooled slowly or by inversion of titanomaghemite during heating. Having a 70 percent iron content and being abundant, it is the most important iron ore. By weight, pure hematite consists of about 70% iron and 30% oxygen. Much like most natural materials, it is rarely found with that pure composition. α-Fe_2O_3 crystallizes in the rhombohedral system with space group R-3c and lattice parameters a = 5.0369 Å and c = 13.749 Å [14]. In addition to the N´eel temperature, it can display the Morin temperature, the blocking temperature and the freezing temperature [15].

1.2.2 Zinc Oxide (ZnO)

At room temperature, zinc oxide (ZnO) is a group II–IV semiconductor with a wide band gap of 3.37 eV [16,17] and large exciton binding energy (60 MeV) [18]. Depending on the reaction conditions, zinc oxide can be synthesized as rods, cones, bullets and hexagonal plates, making it a remarkably versatile semiconductor nanomaterial [19]. The properties of ZnO nanoparticles are governed by their size, shape, surface area, crystallinity, and stability, which depend on the synthesis methods and conditions [20]. ZnO crystallizes as a thermodynamically stable hexagonal wurtzite structure, with basal plane parameter a and axial lattice parameter c, having a ratio of c/a = 1.633, and is built from two interpenetrating hexagonal close-packed (hcp) sub-lattices of one type of atom that are displaced along the three-fold c-axis by u = 3/8 = 0.375c.

A sublattice of ZnO consists of four atoms per unit cell, i.e., the ZnO unit cell contains 4 Zn and 4 O atoms and the wurtzite structure has three surfaces of particular importance, namely (0001), (1120), and (1100) planes (c, a, and m-planes, respectively) [21].

1.2.3 Zinc Ferrite ($ZnFe_2O_4$)

A zinc ferrite is an inorganic compound that consists of zinc and iron (ferrite) and has a general formula of $Zn_xFe_{3-x}O_4$. $ZnFe_2O_4$ is a spinel-structured ferrite with a narrow bandgap (−1.9 eV) with low activation energy, high surface activity, high electron mobility, excellent stability, high thermal conductivity, high electrical resistivity, controllable saturation magnetization, moderate thermal expansion coefficients, energy transfer efficiency and narrow line width in ferromagnetic resonance [22–24]. In addition to its normal spinel structure, it crystallizes in a regular system ($a = b = c$, $\alpha = \beta = \gamma = 90$).

1.3 Hollow structured materials

The word ‘‘hollow” refers to an empty space or cave inside. Structures containing vacant spaces inside can be considered hollow [25]. However, in material science, hollow generally refers to structures with an open and large fraction of empty space along with well-defined shells [26]. Nanomaterials with hollow structures fall into a special category of materials characterized by solid walls enclosing an internal void. These materials come with certain advantages compared with their bulk counterparts. Hollow nanomaterials have dramatically increased surface areas compared to bulk material, which makes hollow nanomaterials extremely useful in surface-related applications [27]. These materials require significantly lower amounts of expensive noble metals, representing a noble-metal economic design.

Hollow materials generally show enhanced light scattering, faster surface reactions, and lowered charge recombination. Besides, the hollow spheres are constructed with an unusual hierarchically nanoporous structure, which enables more efficient transport of the reactant molecules to reach the active sites on the framework walls. Aside from that, the hollow spheres permit multiple reflections of UV-visible light inside the cavity that promotes more efficient use of the light source. Additionally, hollow spheres can be easily separated from slurry systems through filtration or sedimentation, and can be reused more efficiently than nanosized powder photocatalytic materials [28]. The massive pores and high porosity of hollow structured materials indeed decrease the density of the absorber, affording the lightweight features for practical application [29].

1.3.1 Synthesis of hollow structured materials

1.3.1.1 Template-assisted method

Depending on the type of template used for fabricating the hollow core, this method can be classified as hard-templating or soft-templating. Hard-templating uses rigid particles as core templates that are removed after the formation of a core-shell to obtain a hollow structure. Silica, carbon spheres and polystyrene spheres are generally used as hard templates. It is possible to control the morphology, particle size, and structure of nanomaterials using these methods. As for these approaches, a brief synthesis process can be exhibited in the following three steps [30]:

a. Fabrication of template materials with specific morphologies as kernel support materials,
b. Depositing the target material on the surface of the template materials,
c. Removing the interior template materials through appropriate approaches to obtain the hollow nanostructured materials.

Soft templating, however, generates hollow structures directly by the self-assembly of starting materials. Polyvinyl pyrrolidone (PVP), cetyltrimethylammonium bromide (CTAB), sodium dodecyl sulfate (SDS), vesicles, droplets, micelles and gas bubbles are widely used soft template materials. The surfaces of these templates are curved or spherical under the action of surface tension since they are primarily formed in solution and are relatively soft and therefore, suitable for preparing hollow spheres.

It is true that hard template strategies for hollow structured materials are simple and straightforward to apply, but the strategies are only applicable to core-shell structures where the core and shell exhibit significantly different dissolution properties. A soft template approach, on the other hand, allows the soft template to be easily removed from core-shell structures.

However, the use of a soft template strategy restricts the morphology of hollow structures to mainly spherical shapes due to inherent difficulties in modulating the soft template. Besides, the conditions in which these templates are created are usually affected by factors like temperature, pressure, pH, concentration, etc. As a result, it is important to explore hollow structures with different compositions based on the specific situation.

1.3.1.2 Template-free method

A hollow sphere can be prepared without using an additional template. The template-free method can be mainly divided into two categories such as self-templating and self-assembly methods. An unstable intermediate obtained during the reaction acts simultaneously as both a hard template and a sacrificial template in the self-template mechanism.

A template-free strategy may be more convenient in some cases since they are generally one-pot processes without additional etching steps. Nonetheless, finding the right conditions for unstable intermediates such as organized crystallite aggregates, concave octahedra with high surface energy, and self-templates remains challenging. Further, the mechanisms underlying the transition from unstable kinetic intermediates to stable thermodynamic hollow structures have still not been properly elucidated.

1.3.1.3 Spray drying method

In this method, nanoparticles are suspended in related solvents as a precursor solution. Spray drying consists of transforming a fluid into dried particles by using a gaseous hot environment. Different stages of the spray-drying process involve atomization, droplet-to-particle conversion and particle collection. It is often necessary to add some chemicals to adjust the pH of nanoparticulate suspensions in order to maintain their colloidal stability.

1.3.1.4 Kirkendall method

It is possible to readily convert solid nanoparticles into hollow spheres in some cases instead of hard templating. Under controlled heating conditions, the Kirkendall effect converts low-density materials like hydroxides to high-density ones like oxides. According to conventional Kirkendall theory, the fast diffusing materials create voids around the slower diffusing ones to compensate for the unequal material flow [31]. As part of the nanoscale Kirkendall forming process, small voids are produced at the interface, enhanced by atom diffusion, and thus form hollow cavities [32].

1.3.1.5 Ostwald ripening

Ostwald ripening is a phenomenon which is evident in solid solutions or liquid sols. The process involves dissolving small crystals or sol particles and re-depositing them as crystals or larger sol particles. This phenomenon is commonly observed in oil-in-water emulsions. Since the inner crystallites develop at the earliest stages of crystallization and growth, they are usually smaller and have higher surface energy than the outer crystallites [33]. Smaller particles, due to significant differences in interfacial energy, gradually dissolve and redeposit on the surface of large particles during crystallization, leading to the continued growth of larger particles and the dissolution of smaller particles [34].

1.3.1.6 Ion exchange

In ion exchange, cations or anions are exchanged between a solution and a solid. The Ion exchange process has been widely used to fabricate hollow nanostructured materials [35–37]. In general, hollow nanostructured materials prepared through ion exchange are largely determined by the morphology of the precursor materials. A large number of hollow nano- and microstructures have been reported including single, double, triple, quadruple shelled structures by using this ion exchange process [38].

1.3.1.7 Selective etching

Through chemical etching or direct calcination, the selective etching strategy creates cavities by selectively etching some constituent materials [39].

1.3.1.8 Galvanic replacement

Hollow nano- and microstructures can be assembled using galvanic replacement reactions, which are simple but versatile. Using this method, Xia et al. [40] created hollow nanostructures of Au, Ag, Pd, and Pt with controlled and well-defined thicknesses and pore volumes. The reaction is triggered when metal particles came into contact with other ions of a higher reduction potential [41]. A difference in electrical potential between two metals drives this force [42].

1.3.2 Advantages of template assisted method

Template-assisted synthesis is an effective method for exactly controlling the morphology of hollow structures. This can be accomplished by choosing templates with different shapes and/or varying operational parameters. Several studies have confirmed that the hard template method is the easiest to control and that it can be used to precisely adjust the shape and composition of hollow structures.

1.3.3 Difficulties with soft template

A soft template is particularly sensitive to the parameters of synthesis, such as temperature, pH, solvent polarity, etc., so controlling certain structural features of hollow materials, such as particle size, shell thickness, and particle morphology, can be challenging.

1.3.4 Carbon template-assisted synthesis of hollow structured materials

Carbon spheres are among the most commonly used hard template materials due to their precise synthesis, tunable size, surface properties, and ease of removal. Porous carbon, graphene, carbon tubes, and other types of conductive carbon can be used as template materials.

In a conventional hard templating process, there are three main steps: the first is the formation of the template material, the second is the deposition of precursors for the hollow material to be cast, and the third is the removal of the template. But, in our study, we adopted a one-pot synthesis approach where the carbon template was in-situ formed under hydrothermal conditions and a separate template formation was not required.

1.3.5 Recent advances in hollow structured materials

1.3.5.1 Hydroxide hollow structures

Single transition metal hydroxides, layered double hydroxides, and oxyhydroxides are the most common hydroxides. Transition metal hydroxides have become a class of very promising materials because of their outstanding catalytic activity, high abundance, miscellaneous chemical compositions, and environmental friendliness [43,44]. As a special hydroxide, layered double hydroxides (LDHs) are ionic lamellar structures, which are formed from brucite-like layers and interlayer anions and water molecules [45]. The application of oxyhydroxides such as NiOOH, FeOOH, CoOOH, etc., has received a great deal of experimental and theoretical attention in the last few years. [46–48]

1.3.5.2 Transition metal oxide hollow structures

Because of the unique chemical composition and crystal structure, such as spinel, perovskites, layered oxides, etc., transition metal oxide hollow structures have been extensively used [49]. A variety of oxide hollow structures like hollow nanotubes [50], hollow spheres [51], hollow nanosheets [52], hollow polyhedrons [53], etc. have been synthesized, and their unique structural features equip them with special properties to make them useful for applications in different fields.

1.3.5.3 MOFs-based hollow structures

In recent years, metal-organic frameworks (MOFs), a type of periodic network structure made of metal ions and organic ligands, have attracted special attention due to their unique structural characteristics, including large specific surface areas, highly ordered micropore structures, uniform pore sizes and special shapes, and abundant active sites, among others. [54,55]. Micropores constitute the majority of pores in MOFs. Consequently, the hollow structure of MOFs with large void spaces and mesoporous or macroporous channels exposes more active sites and accelerates material diffusion compared to bulk MOFs.

1.3.5.4 Phosphate-based hollow structures

Transition metal phosphates have recently attracted researchers' attention because of their low cost, environmental friendliness, and unique tunable structure [55]. Typically, transition metal phosphates have an open framework with a layered structure, which makes electron and ion transfer easier [56].

Additionally, the transition metal ions with variable valence can optimize the redox behaviour while the phosphate group can provide many protons to facilitate good proton conductivity through the interlayer region.

1.3.6 Factors influencing the morphology of hollow structured materials

1.3.6.1 Time

A key parameter in the synthesis process of hollow nano- and microstructures is time. Research has shown that the etching time, reaction time, and calcination/annealing time all have significant effects on the transformation of solids into hollows [57,58].

1.3.6.2 Concentration

Concentrations of solutes and solvents can also influence hollow nano- and microstructure formation. Ma et al. [57] reported the fabrication of self-templated Fe-glycerate hollow spheres via a solvothermal method by tuning the reaction time and their research revealed that at different time scales, various stages of hollow structure formation happened.

1.3.6.3 Temperature

In the fabrication of hollow structures, the reaction or annealing/calcination temperature plays a significant role. It was evident from several studies that annealing temperature influences the shell thickness, cavity radius, surface property, crystallinity and porosity of materials [59,60].

1.3.7 Factors influencing the performance of hollow structured materials

1.3.7.1 Shell number (single, double, multiple)

One of the most distinguished features of hollow structures is the number of shells. Single, double, and multi-shell hollow structures have their own set of properties. TEM is the most useful tool for determining how many shells are present in hollow structures. Several factors can affect the shell number, including the type of solvent, reaction time, composition, and concentration of precursors [61].

1.3.7.2 Shell size, thickness and inter-shell spacing

In addition to shell number, shell size, thickness, and inter-shell spacing have a significant impact during hollow structure formation and have a substantial influence on performance.

Size, thickness, and inter-shell spacing of shells play a crucial role in short transport pathways and volume expansion. It is generally expected that smaller inter-shell spacings and more shells will provide better performance.

However, it is also important to consider the grain size and porosity of shells. A porous structure provides a large surface area for the active materials, excellent contact with the electrolyte ions, and a short pathway for the ions and electrons. Shells made up of smaller grains have been shown to have more surface area [62]. In the template-assisted method, the outer shell size is partially determined by the template [63]. Inner shell size, however, is dependent on the formation conditions [64].

1.3.7.3 Morphology

A hollow structured material's shape and nature also affect its performance in different applications. The following aspects are important for hollow nanostructured materials:

1.1 Easy penetration of electrolyte into the interior surfaces through porous shells [65],

1.2 Improved surface area and excellent stability due to protective outer shell [66], and

1.3 Enhanced ions/electrons transport for fast kinetics provides a means for enhanced electrolyte contact with active materials [67].

One of the great interests of materials scientists and engineers is controlling the shapes and morphology of hollow structures and understanding how ions interact within them.

1.4 Applications of hollow structured materials

Hollow structured materials have promising applications across a wide array of scientific fields including catalysis [68], energy storage [69], magnetic resonance imaging [70], cancer imaging therapy [71], sensors [72], drug delivery [73], and environmental remediation [74].

1.4.1 Photocatalysis

Photocatalyst is composed of two words: photo, which refers to photons, and catalyst, which refers to substances that influence reaction rates. A photocatalyst is therefore a material that changes the rate of a chemical reaction when exposed to light and this phenomenon is known as photocatalysis. Almost all photocatalysts are semiconductors. A photocatalytic reaction uses light and a semiconductor to carry out a reaction, in which an electron-hole pair is generated on exposure of a semiconducting material to light. In terms of the physical state of the reactants, photocatalytic reactions can be divided into two categories. Homogeneous photocatalysis occurs when the semiconductor and reactant are both in the same phase, i.e. gas, solid, or liquid. It is called heterogeneous photocatalysis when the semiconductor and reactant are in different phases.

Photocatalysis has been demonstrated to be an eco-friendly and sustainable method for removing dyes from wastewater [75]. It is important to note that in photocatalytic processes, electron and hole generation are two competing processes, and photocatalytic activity depends heavily on electron and hole lifetimes [76].

In addressing energy and environmental challenges, photocatalysis promises a bright future. In photocatalysis, the efficiency of light harvesting, the separation of charges, and the acceleration of surface reactions are heavily dependent on the design of photocatalysts.

A semiconductor with a hollow structure offers many advantages when developing photocatalysts, including enhanced light scattering and harvesting, shortened distances for charge migration, directed charge separation, and an abundance of surface reactive sites [77].

1.4.2 Energy storage devices

Currently, lithium-ion batteries are among the most popular electrochemical energy storage devices for electronic vehicles and portable devices due to their environmental friendliness, high energy density, and extended lifespans [78]. There have been numerous studies on nanomaterials with porous nanoarchitecture for use as LIB electrodes. Hollow nano- and microstructures have dominated the research due to their low density, high surface area, and high loading capacity [79].

1.4.3 Dye-sensitized solar cells

The severe environmental problems resulting from the burning of fossil fuels and society's future energy demands prompted researchers to study clean energy devices such as dye-sensitized solar cells (DSSCs). Studies by Xu et al. [80] revealed that hollow materials are superior to conventional Pt-based cells in terms of power conversion efficiency.

1.4.4 Water splitting

Energy consumption is rising day by day because of an increase in population and an increase in energy demand. Direct splitting of water into oxygen and hydrogen is one of the most desirable methods for converting and harvesting solar energy [81]. It has been reported that a large number of metal oxides, metal sulfides, metal nitrides, metal phosphides, and their composites have been used for water splitting. Rapid advances in this field have improved the performance of photocatalytic water splitting, but low efficiency limits their practical use.

As an alternative to noble metal-based catalysts, hollow nanostructured materials exhibit good conductivity, excellent electrical conductivity, and intrinsic electronic structures that facilitate hydrogen and oxygen evolution at high efficiency [82].

1.4.5 Low-temperature chemiresistive sensing

The use of hollow-/microstructures for low-temperature chemiresistive sensing applications has also been found to be significant in addition to the above applications. Compared with single component-based nanodevices, mixed quaternary metal oxide hollow spheres demonstrated improved response and stability [83].

1.4.5 Drug delivery

The high drug loading capacity and chemical/thermal stability of hollow structured nanomaterials make them promising candidates for drug delivery [84].

1.4.6 Gas sensing

The resistance change of sensing materials is mainly caused by the interaction of target gases with oxygen species on their surfaces, which is a surface reaction process; hence, the composition and morphology of sensing materials have a strong relationship with sensing performance [22]. The hollow nanostructure offers large surface areas and fast air/gas penetrations to the interior cavity. Meanwhile, the enlarged surface prevents the gas from leaving the hollow structure [23].

CHAPTER 2

Hydrothermal synthesis, characterization and thermal stability studies of α-Fe_2O_3 hollow microspheres

Abstract

A simple, cost-effective hydrothermal technique was used in this study to successfully fabricate hollow α-Fe_2O_3 microspheres, using only fructose and anhydrous ferric chloride without any organic solvent or additive. The synthesized α-Fe_2O_3 hollow microspheres were characterized by X-ray diffraction spectroscopy (XRD), field-emission scanning electron microscopy (FE-SEM), energy-dispersive X-ray spectroscopy (EDX), transmission electron microscopy (TEM), X-ray photoelectron spectroscopy (XPS), and attenuated total reflectance Fourier-transform infrared spectroscopy (ATR-FTIR). Based on the results, the shell was composed of aggregated α-Fe_2O_3 nanoparticles, while the fructose-derived carbon core was decomposed during calcination, leaving a hollow interior. XRD analysis confirmed the presence of the α-phase and the absence of γ-phase Fe_2O_3. A mean diameter of 595 nm was estimated for the microspheres by the Gaussian fit of the histogram constructed from the diameters measured over the SEM images. EDX spectrum of the sample showed signals attributed to Fe and O, and a homogenous distribution of these elements was confirmed by elemental mapping studies. ATR-FTIR analysis confirmed the bending and stretching vibration modes of the Fe-O bond. TGA-DTA data depicted that thermal stability of α-Fe_2O_3 hollow microsphere was achieved at 480 °C and no weight loss was observed up to 1000 °C. High-temperature calcination results showed that the material can maintain its hollow morphology up to 700 °C. This material has potential applications in drug delivery, gas sensing, and lithium storage.

2.1 Introduction

Hematite (α-Fe_2O_3) is an n-type semiconductor that has a bandgap of 2.1 eV and is the most stable form of iron oxide [85]. Because of its availability, nontoxicity, low processing cost, thermal stability, environmental friendliness, sensitivity to visible light and good corrosion resistance, it has gotten a lot of interest in numerous fields. [27,86]. α-Fe_2O_3 has been extensively investigated for its use in catalysis [87][88], photocatalytic oxygen evolution [89], gas sensing [85,90], optical devices [91], supercapacitor electrodes [92], lithium-ion batteries [86,90,93], electromagnetic devices [27], water treatment [94], and biomedicine [95].

Hematite with a hollow structure is more intriguing to researchers because of its excellent surface permeability, low density, and high surface area compared to ordinary hematite [90]. To date, many researchers have reported the synthesis of hematite; however, not many have investigated the fabrication of hematite hollow spheres. Hollow nano/micro-structures of α-Fe_2O_3 have reportedly been prepared by a variety of synthetic methods, including sol-gel synthesis [96], centrifugal spinning [97], electrospinning [98], wrap–bake–peel processing [89], quasi emulsion-template [99], gas-bubble template [100], hydrothermal [86,93,101], and solvothermal [87,102,103] methods.

The hydrothermal method is, by far, the most widely used method for fabricating hollow α-Fe_2O_3 nano-/micro-structures because of its high yield and simplicity [86]. Ma et al. used a hydrothermal approach utilizing an inside-out-outside-in Ostwald ripening strategy to produce double-shell hollow hematite nanoparticles [104].

Vuong et al. synthesized hollow nanospindles of α-Fe_2O_3 by a hydrothermal technique, and their ethanol-sensing properties were investigated at different gas concentrations and temperature levels [85]. Niraula et al. synthesized shape-controlled α-Fe_2O_3 hollow nanorings (NRs) and nanotubes (NTs) via a microwave-assisted hydrothermal process [105]. In an HF aqueous system, Qiu et al. hydrothermally synthesized hollow polyhedral α-Fe_2O_3 utilizing 1,3,5-benzenetricarboxylic acid as an additive [88].

Although there have been some reports on the fabrication of hollow α-Fe_2O_3 microspheres by hydrothermal techniques, most of these methods involve the use of expensive and harmful additives and solvents, complex multistep synthesis procedures, and individual synthesis of core and shell materials. Moreover, to the best of our knowledge, stability of α-Fe_2O_3 hollow structure at higher temperature has not been investigated before. Hollow structures have a broad range of potential applications due to their higher surface area, larger pore size, and lighter weight. Therefore, a cost-effective fabrication process is necessary to maximize their utilization. To this end, herein, we describe a straightforward method to fabricate α-Fe_2O_3 hollow microspheres by a simple, facile, cost-effective one-pot hydrothermal process and study their thermal study at higher temperatures.

2.2 Experimental

2.2.1 Materials

Ferric chloride (anhydrous), used as the hematite precursor, was procured from Kanto Chemical Co. Inc. (Japan).

As the precursor of the carbon template, D-Fructose was supplied from Sigma-Aldrich (USA). Both chemicals were analytically pure and were not further purified during the experiment.

2.2.2 Preparation of α-Fe_2O_3 hollow microspheres

0.2 M $FeCl_3$ and fructose ($C_6H_{12}O_6$) were dissolved in a 50 mL aqueous solution. The solution is then filled to a 100 ml Teflon-lined stainless-steel autoclave to heat at 180 °C for 16 h. Afterwards, the product after hydrothermal treatment was washed in water and ethanol. The washed product was then dried in air at 60 °C for 16 h, then vacuum dried for another 5 h. Calcination at 500 °C for 3 h provides hollow α-Fe_2O_3 microspheres.

2.2.3 Preparation of carbonaceous spheres

A 0.2 M fructose solution was obtained by dissolving fructose in 50 mL of deionized water. The solution was then heated to 180 °C for 16 h in a 100-mL Teflon-lined stainless-steel autoclave. Afterwards, the product was washed with water and ethanol, dried at 60 °C for 16 h and then vacuum dried for another 5 h.

2.2.4 Characterizations

Powder XRD patterns of the samples were acquired on a Rigaku Ultima IV diffractometer to determine the crystallinity of the α-Fe_2O_3 hollow spheres.

The surface morphology and elemental distribution were analyzed by field-emission scanning electron microscopy (FE-SEM S-4500, Hitachi Ltd., Japan) and energy-dispersive X-ray spectroscopy (FE-SEM.EDX S-782XII, Horiba Ltd., Japan). The shell thickness of hollow α-Fe_2O_3 microspheres was measured using TEM (JEM-2010, JEOL Ltd., Japan). A JASCO ATR PRO450-S FTIR-ATR instrument was used to detect the presence of Fe-O bonds.

The specific surface areas were measured by a NOVA 1200e surface area and pore size analyzer applying Brunauer-Emmett-Teller (BET) method. Fe 2p and O 1s were detected with the XPS (PHI 5000 VersaProbe II (ULVAC-PHI INC.)). Thermogravimetric/differential thermal analysis (TGA/DTA) measurements were made in the air atmosphere using a Rigaku Thermo Plus Evo II TG-DTA 8122 for the sample temperature up to 1000 °C.

2.3 Results and discussions

Hollow hematite microspheres were successfully prepared using a hydrothermal technique [106] with $FeCl_3$ anhydrous as the α-Fe_2O_3 precursor and fructose as a sacrificial carbon template. The synthesis process is quite simple involving two basic steps (Fig. 2.1).

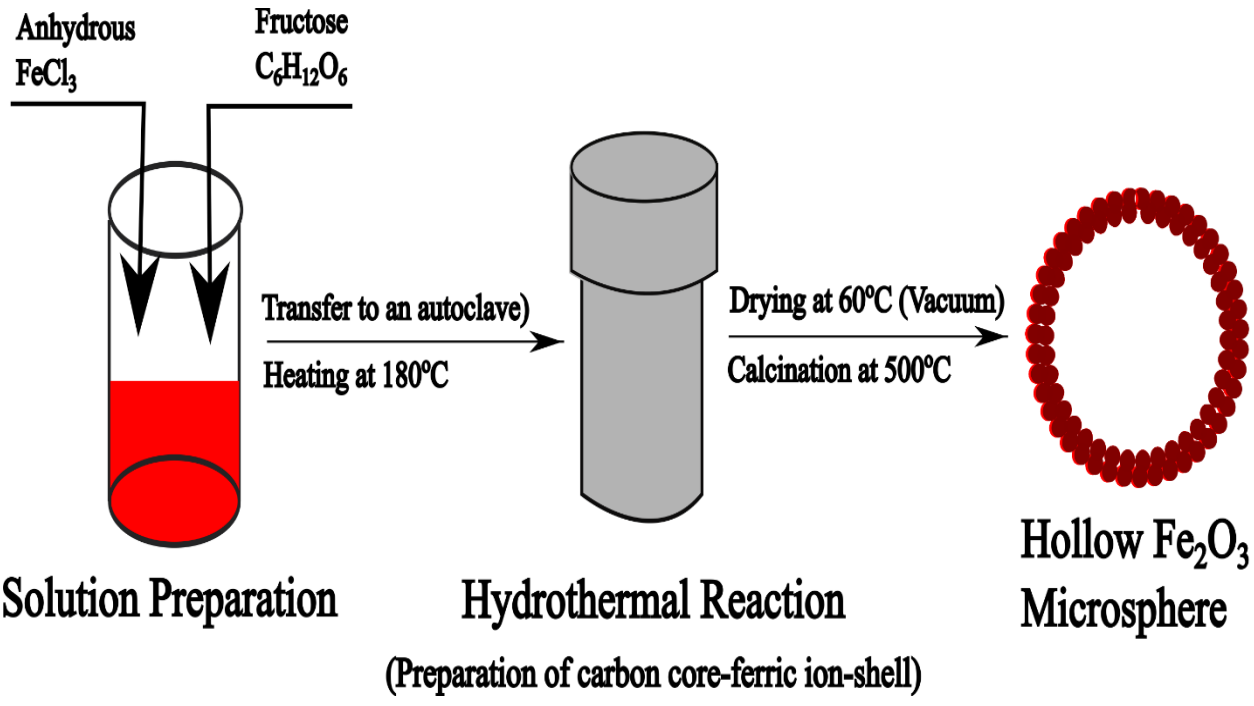

Fig. 2. 1: *Schematic representation of hollow α-Fe_2O_3 synthesis by applying a hydrothermal technique*

A core@shell composite is first formed during the heat treatment of $FeCl_3$ and fructose at 180 °C. Due to the pressure developed in the autoclave, fructose is converted to carbonaceous spheres through the dehydration reaction. These carbonaceous spheres possess oxygen-containing functional groups such as -OH and C–O [106] which attract the metallic cations. These electrostatic interactions or co-ordination between the carbonaceous spheres and adsorbed metallic ions trigger the construction of the core-shell composite.

Hollow microspheres of α-Fe_2O_3 are produced through the elimination of the carbon core during the calcination process. In the process, several layers of dense nanoparticles are produced while the carbon core oxidizes and decomposes, leaving a hollow interior. The carbonaceous template serves as a shape-directing agent [107] and its surface performs a significant role in the α-Fe_2O_3 hollow structure formation.

The phase composition of the fabricated α-Fe_2O_3 hollow microspheres was investigated by XRD analysis. As illustrated in Fig. 2.2a, it has been observed that the α-Fe_2O_3 sample exhibits sharp peaks at 24.1°, 33.1°, 35.6°, 40.8°, 49.5°, 54.0°, 57.5°, 62.4°, 64.0°, 71.9° and 75.4°. All peaks are indexed to the α-Fe_2O_3 phase (JCPDS No. 01-089-0596) [108]. The diffraction peak at 33.1° corresponds to the lattice plane of (104) [88]. No broad peak at 27.3° corresponded to the diffraction peak (116) of γ-Fe_2O_3 [105] confirms the absence of any γ-Fe_2O_3.

No other impurity peaks indicate that the samples were highly crystalline and of high purity. Applying the Debye-Scherer equation [109], the average crystal size was measured to be 35.4 nm.

Bare and ferric ion-coated carbonaceous spheres (Fig. 2.2b) display almost similar broad peaks of carbon at approximately 20°. No strong peaks were observed at 2θ = 20°–30° with the XRD spectrum suggesting that carbon is amorphous [16].

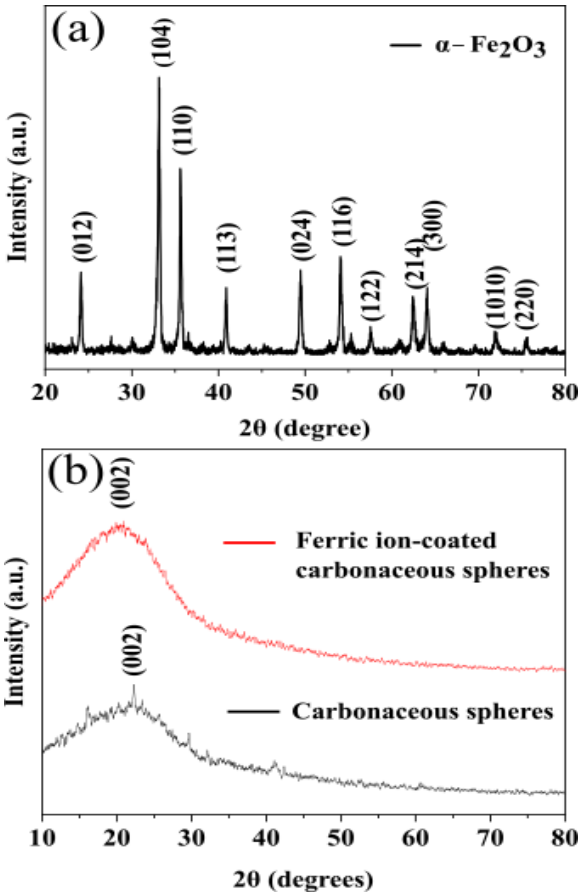

Fig. 2. 2: *XRD patterns of (a) hollow α-Fe_2O_3 microspheres calcined at 500 °C; (b) bare carbonaceous spheres and ferric ion-coated carbonaceous spheres*

To investigate the preparation of bare carbonaceous spheres, we performed the same synthesis experiment without using the Fe precursor (anhydrous $FeCl_3$) and succeeded in synthesizing carbonaceous spheres that have an average diameter of 661 nm. Morphologies of the as-prepared carbonaceous spheres and the hollow α-Fe_2O_3 microsphere samples were analyzed using SEM.

Fig. 2.3 (a-b) display SEM micrographs of the carbonaceous spheres, showing that spherical carbonaceous spheres have sizes in the range of 400–900 nm. A large increase in diameter was observed in the ferric-ion-coated carbonaceous sphere. Fig. 2.3 (c-d) show that the surfaces of the spheres were rough compared to those of the carbonaceous spheres synthesized without Fe precursors.

SEM micrographs of the α-Fe_2O_3 hollow microspheres are presented in Fig. 2.3 (e-f), which show that nanosized α-Fe_2O_3 particles were formed, aggregating to form the shell of the hollow microspheres. It is also evident that the shape of the microspheres was slightly deformed, owing to the random evaporation of carbonaceous materials from the core during calcination and almost all microspheres have a hollow interior. The diameter of the hollow spheres was also reduced considerably. The shell thicknesses of the hollow α-Fe_2O_3 microspheres were found to be 40–150 nm, as measured from the TEM images (Fig. 2.3 (g-h)).

The histograms for the diameters of the carbonaceous spheres (Fig. 2.4a), ferric-ion-coated carbonaceous spheres (Fig. 2.4b), and hollow α-Fe_2O_3 microspheres (Fig. 2.4c) were constructed by SEM image particle size analysis, and their average diameters were found to be 661 nm, 3.56 μm, and 595 nm, respectively, from the Gaussian fit of the histograms.

The histograms also show that the α-Fe_2O_3 hollow microspheres have a smaller average diameter than the carbon cores and ferric-ion-coated carbonaceous spheres. This is because of the 'shrinkage' effect [106] during calcination, which occurs when metal-ion-rich shells decompose and transform into a hollow metallic oxide layer. For the same reason, we see a much wider distribution of diameters in the α-Fe_2O_3 microspheres than in the carbonaceous spheres.

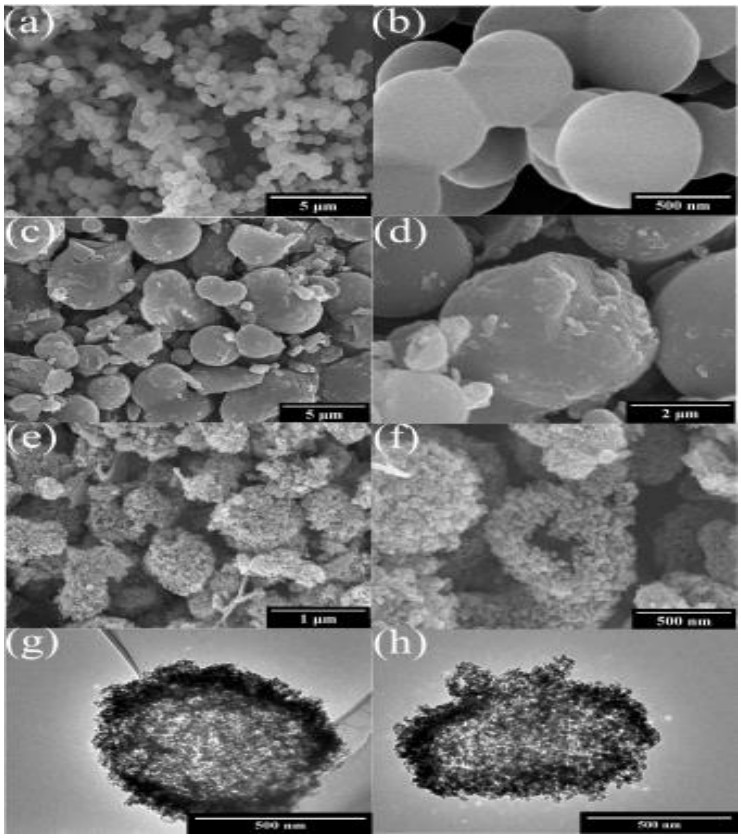

Fig. 2. 3: *(a-b) FE-SEM images of carbonaceous spheres prepared without an iron precursor, (c-d) FE-SEM images of ferric ion-coated carbonaceous spheres before calcination, (e-f) FE-SEM images of hollow α-Fe_2O_3 microspheres, and (g-h) TEM images of hollow α-Fe_2O_3*

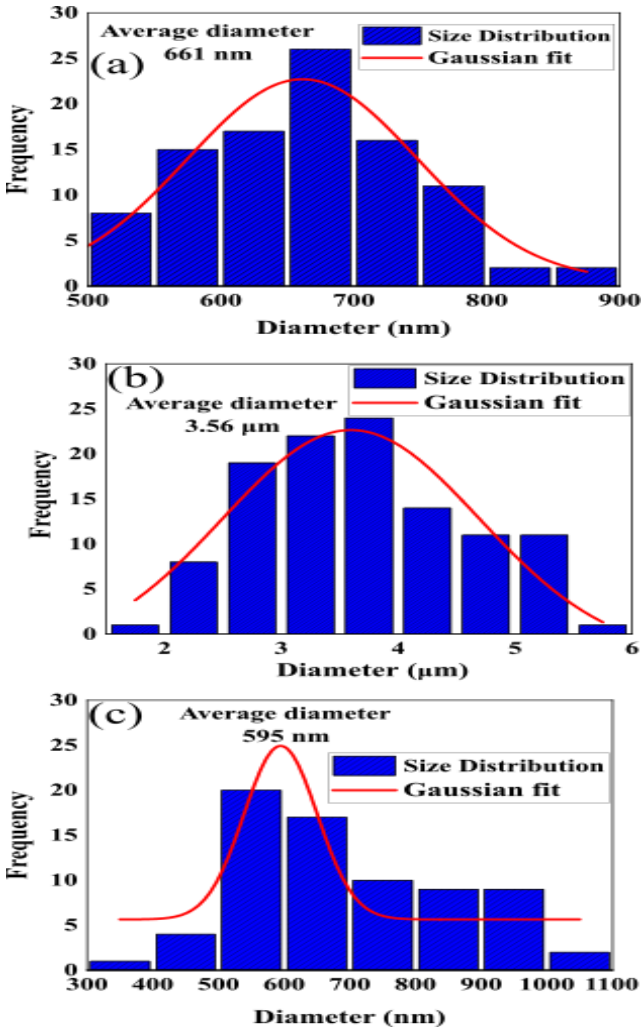

Fig. 2. 4: *Average particle size distributions of (a) carbonaceous spheres and (b) ferric ion-coated carbonaceous spheres before calcination, and (c) hollow α-Fe_2O_3 microspheres*

To investigate the elemental composition of hollow microspheres made of α-Fe_2O_3, EDX measurements were utilized. Fig. 2.5a shows the peaks of Fe and O. Elemental mapping (Fig. 2.5 (b-d)) was performed to observe the elemental distributions.

As expected from the mapping analysis, elements Fe and O showed complete coverage of the image frame and were distributed homogenously in the Fe_2O_3 structure. The corresponding mass and atomic percentages obtained from the EDX analysis are also shown in Table 2.1.

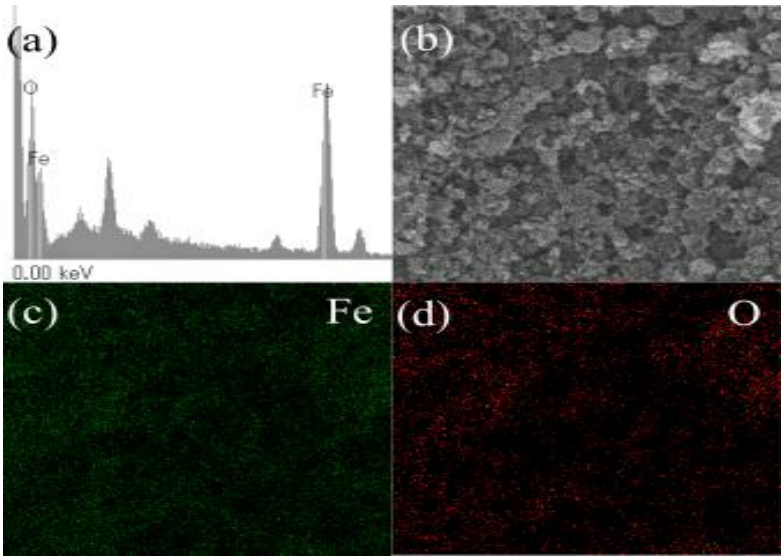

Fig. 2. 5: *(a) EDX spectrum of hollow α-Fe_2O_3 microspheres, (b) selected mapping area, (c-d) elemental distributions of Fe and O, respectively*

Table 2. 1: *Elemental composition of the prepared hollow α-Fe_2O_3 microspheres obtained by EDX analysis*

Element	%Mass	%Atom
Fe	64.66	34.39
O	35.34	65.61
Total	100	100

XPS analysis was conducted to assess the surface chemical composition of the hollow α-Fe_2O_3 microspheres. Fig. 2.6a presents the wide spectrum, showing the signals of Fe, O, and C. The peak at 710.2 eV typically corresponds to Fe $2p_{3/2}$ [86][97], whereas that at 723.9 eV is assigned to Fe $2p_{1/2}$ (Fig. 2.6b) [110]. These peaks, together with the satellite peaks at 715.1 eV and 730.5 eV, confirm the formation of the hematite phase [97].

Fig. 6c shows that the C-1s spectrum can be deconvoluted to two peaks positioned at 284.6 eV and 288.5 eV, corresponding to C–C sp^2 and O–C=O bonds, respectively. These carbon-containing bonds may originate from the carbon tape used during the XPS sample preparation.

The deconvolution of O 1s gave two peaks at binding energy 529.5 and 532.6 eV, which are attributed to the bonds Fe–O and C=O, respectively (Fig. 2.6d). The formation of Fe-O bonds can also be verified from the binding energy difference of O 1s and Fe $2p_{3/2}$. Δ_{Fe} has been calculated to be -180.7 which is close to -181.0, attributed to the formation of Fe_2O_3 elsewhere [111].

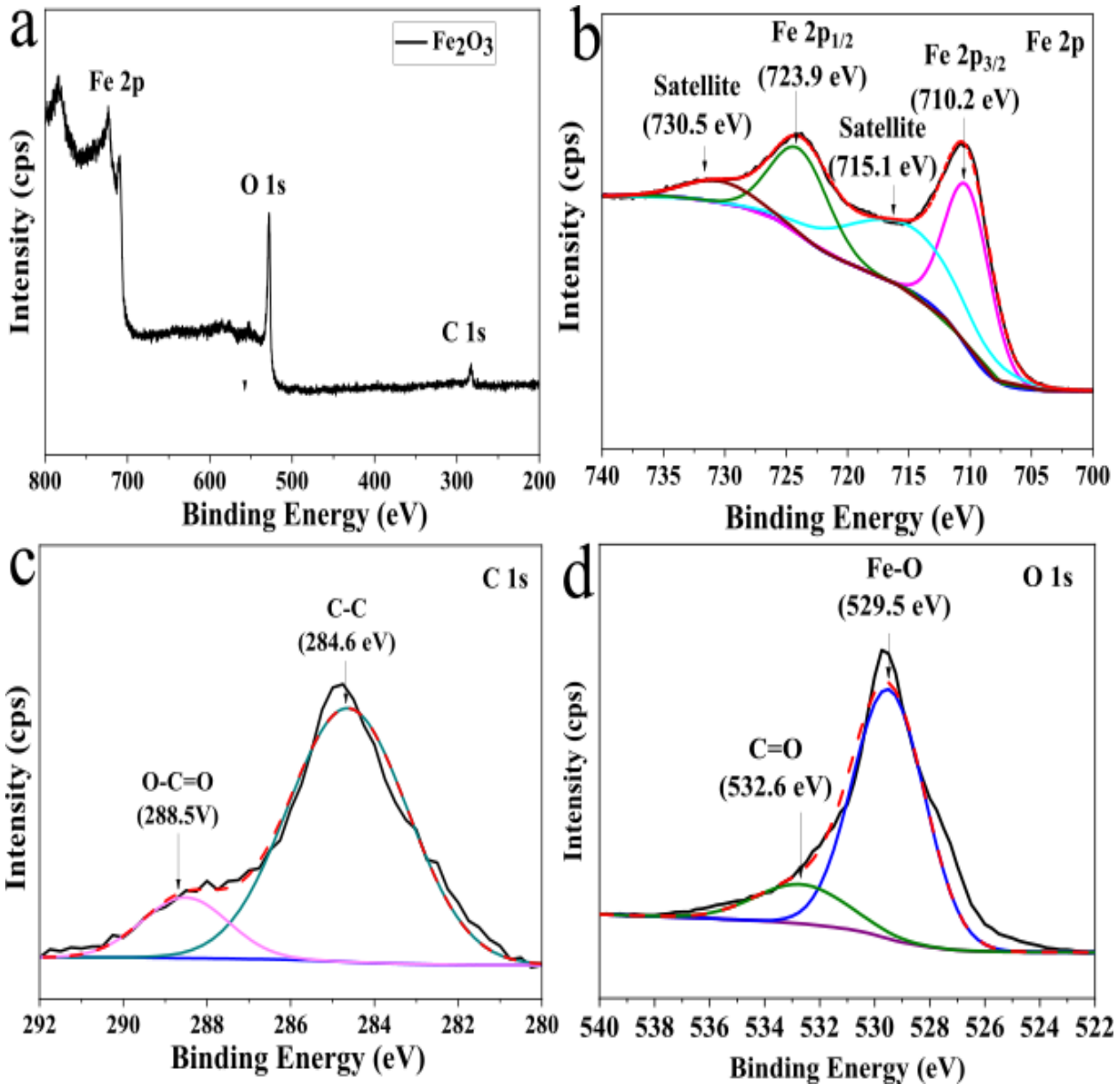

Fig. 2. 6: *(a) XPS wide spectrum of hollow α-Fe_2O_3 microspheres, (b-d) deconvoluted XPS narrow spectra of Fe 2p, C 1s, and O 1s, respectively*

ATR-FTIR was used to analyze the functional groups and to distinguish the purity of the hematite phase. The FTIR spectrum of the α-Fe_2O_3 hollow microspheres is shown in Fig. 2.7.

The significant peaks between 430–530 cm^{-1} and two intense peaks at 435.83 and 520.69 cm^{-1} can be attributed to the bending and stretching modes of the Fe–O bond in a pure α-Fe_2O_3 sample with good crystallinity [112,113].

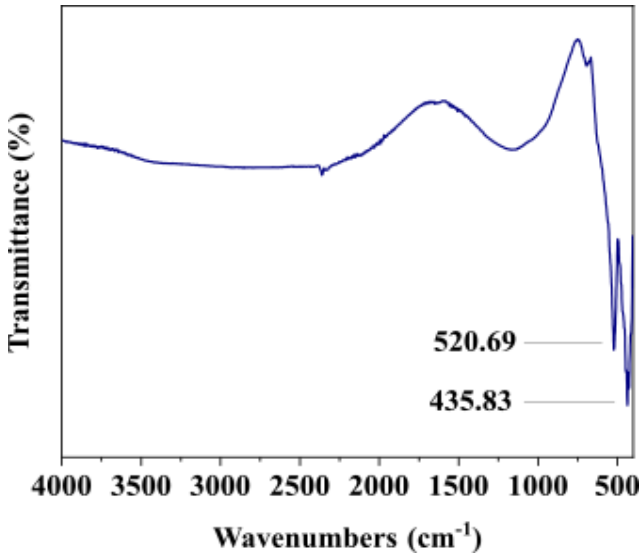

Fig. 2. 7: *FT-IR spectrum of hollow α-Fe_2O_3 microspheres*

According to Brunauer-Emmett-Teller calculations (BET), the surface area of the hollow α-Fe_2O_3 microspheres was 28.16 m^2/g. The obtained isotherm (Fig. 2.8) was classified as type III, as per IUPAC [114]. The existence of a small hysteresis in the N_2 adsorption-desorption isotherm is an indication of the capillary condensation phenomenon, suggesting a mesoporous nature [115]. This is also evident from the peak at 3.6 nm in the differential volume vs pore size graph (Fig. 2.8 (inset)) determined by Barrett-Joyner-Halenda (BJH) pore size analysis.

The mesopores may be derived from the intrapores between α-Fe_2O_3 nanoparticles, which make up the hollow α-Fe_2O_3 shell. Besides, pores within the hematite nanoparticles also contribute to the presence of mesopores. The analysis also revealed a wide range of pore sizes up to 280 nm. These macropores may have contributed to the α-Fe_2O_3 hollow interior formation. The pore volume was calculated to be 0.138 cm^3/g by the BJH pore size analysis.

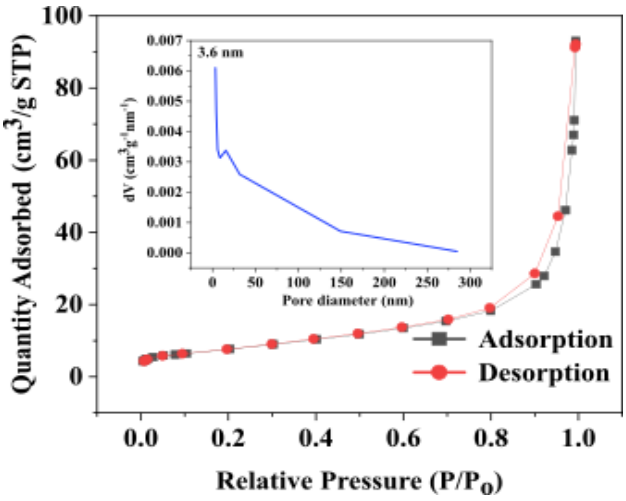

Fig. 2. 8: *N_2 adsorption-desorption isotherm of hollow α-Fe_2O_3 microspheres. Inset shows the differential volume vs. pore size graph constructed from BJH pore size distribution analysis*

Fig. 2.9a shows the results of a TGA combined with DTA in the presence of air and at a heating rate of 10 °C min^{-1} performed on ferric ion-coated carbonaceous spheres. The stability of the weight was experienced at a temperature of 480 °C. The first weight loss of 5.5% at room temperature to 150 °C is primarily because of the evaporation of physically and chemically adsorbed water. The mass reduction of 91.8% between 150 °C and 480 °C may be attributed to the removal of organic materials from ferric ion-coated carbonaceous spheres [116].

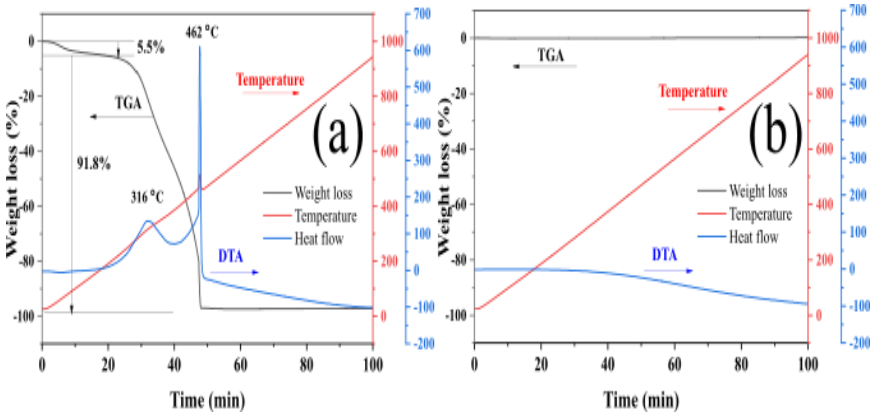

Fig. 2. 9: *TGA/DTA curves of (a) ferric ion-coated carbonaceous spheres (b) hollow α-Fe_2O_3 microspheres*

The low-temperature peak at 316 °C is accompanied by amorphous carbon [117] indicating the combustion of carbonaceous materials. An exothermic peak (462 °C) was detected in the heating process which corresponds to the presence of an α-phase of Fe_2O_3 [118]. Both peaks are exothermic in nature, which may be due to the heat produced during the combustion of organic materials.

On the other hand, the TGA-DTA curve of calcined hollow α-Fe_2O_3 microspheres (Fig. 2.9b) shows no wet loss between room temperature and 1000 °C validating the high thermal stability of the sample.

The calcined sample (at 500 °C) was then re-calcinated for 1 h at the temperature range of 600-1000 °C to evaluate the hollow structural stability of α-Fe_2O_3 microspheres at higher temperatures.

Fig. 2.10 shows the SEM images of α-Fe_2O_3 microspheres at different temperature values. It can be seen that almost all particles retained their hollow morphology at 600 °C (Fig. 2.10 (a-b)). Similar hollow morphology was also observed for α-Fe_2O_3 microspheres calcinated at 700 °C, although the aggregated nanoparticles seemed to be loosened (Fig. 2.10 (c-d)).

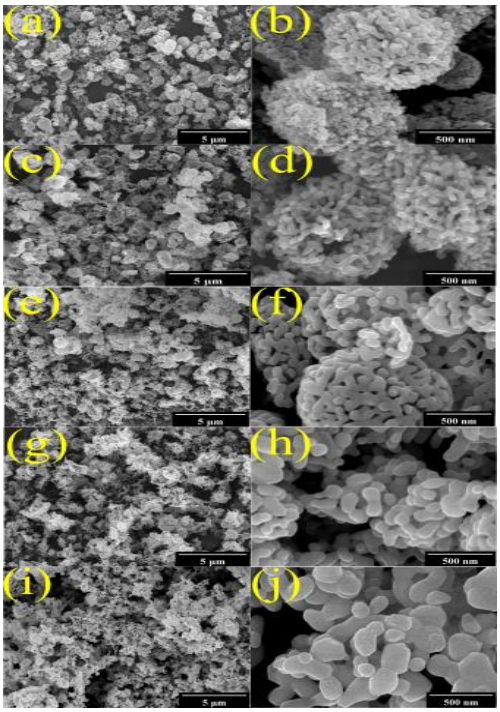

Fig. 2. 10: *SEM images of α-Fe_2O_3 microspheres at different calcination temperatures. (a-b) 600°C, (c-d) 700°C, (e-f) 800°C, (g-h) 900°C, (i-j) 1000°C. Calcination was performed for 1 h*

The collapse of the hollow structure started at around 800 °C as evident from Fig. 2.10 (e-f) and very few α-Fe_2O_3 hollow microspheres were seen at 900 °C (Fig. 2.10 (g-h)). Fig. 2.10 (i-j) display the SEM images of α-Fe_2O_3 hollow microspheres calcinated at 1000 °C where no hollow microsphere has been observed indicating a total demolition of hollow structure morphology.

2.4 Conclusions

A facile hydrothermal method was used in this study to fabricate hollow α-Fe_2O_3 microspheres. In FE-SEM and TEM images, it is demonstrated that obtained samples have hollow interiors and that the hollow microspheres have been formed by the deposition of ferric ions on a fructose-derived carbon core, followed by calcining to decompose the core. The EDX mapping analysis of the sample detected the signals of Fe and O elements. Along with the XRD peak at 2θ = 33.1°, associated with the lattice plane of (104), this confirmed the presence of the α-phase of Fe_2O_3. BET analysis showed that the surface area of the hollow α-Fe_2O_3 microsphere is 28.16 m2/g. TGA-DTA studies confirm the thermal stability of the material up to 1000 °C. Calcination at higher temperatures reveals that the hollow structure starts to collapse at around 800 °C and α-Fe_2O_3 hollow microspheres can retain the hollow morphology up to 700 °C. α-Fe_2O_3 is highly sensitive to the gaseous environment and the hollow structure may offer greater electrolyte accessibility and permit more alterations to the structure. Additionally, the porous shells have high surface areas coupled with high permeability. These outstanding properties highlight the enormous potential this material has for use in gas sensing, lithium-ion storage, and controlled drug delivery systems. Moreover, the fabrication process is simple and can easily be adapted to creating hollow structures of other materials.

CHAPTER 3

Sucrose-derived carbon template-assisted synthesis of zinc oxide hollow microspheres: Investigating the effect of hollow morphology on photocatalytic activity

Abstract

ZnO hollow microspheres were successfully prepared using a sucrose-derived carbon template-assisted hydrothermal method. The synthesized microspheres were characterized by X-ray diffraction, X-ray photoelectron spectroscopy, UV-visible diffuse reflectance spectroscopy, field-emission scanning electron microscopy, and energy-dispersive X-ray spectroscopy. The field-emission scanning electron microscopy results showed that the shell was composed of aggregated ZnO nanoparticles, whereas the sucrose-derived carbon core decomposed during calcination, leaving a hollow interior. X-ray diffraction analysis verified the crystal structure of the ZnO hollow microspheres with a crystallite size of 39.6 nm. ZnO nanoparticles with a similar crystallite size (40.1 nm) were obtained via a polyvinylpyrrolidone-assisted sol–gel method. The photocatalytic efficiency and effect of the hollow morphology of these catalysts for rhodamine blue degradation were studied under ultraviolet light irradiation. Both ZnO hollow microspheres and ZnO nanoparticles showed excellent photocatalytic activity although a minimal amount of these catalysts (only 2 mg) was used in the experiment. The ZnO hollow microspheres showed a 10% higher efficiency than ZnO nanoparticles, owing to their nanoporous structure, higher surface area, and easy formation of •OH radicals.

3.1 Introduction

Rapid industrialization is the primary source of pollutants discharged from effluents. Organic dyes found in textiles, cosmetics, food, and paper products are becoming increasingly prevalent in water bodies [119]. The release of these pollutants into water bodies results in a shortage of clean and fresh water, which is indispensable to the sustainability of human civilization [20]. Some of these dyes, such as methyl orange, rhodamine blue (RhB), naphthalene, and benzidine, are toxic, carcinogenic, or mutagenic to living organisms; therefore, they must be removed from the water bodies before consumption [120]. Photocatalysis, an eco-friendly and sustainable treatment, has shown significant potential for dye removal from wastewater [75]. This type of photodegradation is generally linked to advanced oxidation processes that utilize hydroxyl radicals (•OH) to oxidize organic pollutants [20].

At room temperature, ZnO possesses a large exciton binding energy of 60 MeV [18] and a relatively wide bandgap of 3.37 eV [16,17]. In addition to its high linear refractive index and excellent electron mobility, it has low electrical resistance and high chemical activity [121]. Therefore, ZnO plays a crucial role as a semiconductor photocatalyst owing to its cost-effectiveness, stability, and non-toxicity [18].

The fabrication of hollow-structured photocatalysts has attracted considerable interest in recent years owing to their unique properties, such as enhanced light scattering, fast surface reaction, and reduced charge recombination [122].

Hollow nanoparticles have a larger surface area than bulk nanomaterials, making them particularly useful in surface-related applications [27]. Besides, the larger size of the hollow microsphere is suitable for recovery and reuse in the dye degradation process. Moreover, the interior cavity of a hollow sphere allows multiple reflections of UV-visible (UV-vis) light, allowing more efficient utilization of the light source [28].

Hollow ZnO has been synthesized by different techniques such as the hydrothermal method [121,123], solvothermal method [124], ultrasonic-assisted hydrothermal method [125], chemical vapour-deposition technique [126], one-pot solution method [127], combustion process [128], and in situ gas growth method [129].

Haghighatzadeh et al. prepared ZnO hollow microspheres (ZHMSs) from self-assembled rod-like nanostructures using glycerol as the stabilizing agent [121]. Ju et al. fabricated rambutan-like hierarchical hollow microspheres of ZnO under hydrothermal conditions using carboxyl methyl starch as a soft template [130]. By properly adjusting the concentration of trisodium citrate during the synthetic process, Yin et al. successfully synthesized a variety of ZnO hollow spheres with different surface roughnesses using a template-free one-step hydrothermal method [131]. Liu et al. used a simple seed-assisted hydrothermal technique to prepare ZHMSs on ceramic fibres [132]. Li et al. fabricated three-dimensional nanoarchitectural ZnO hollow spheres via a template-assisted two-step method using ginkgo leaves as a template [133]. Wang et al. used the bubble-assisted Ostwald ripening method to prepare ZnO hollow spheres with a double-yolk egg structure [134]. Nanostructured ZnO hollow microspheres for selective CO_2 reduction were reported by Xue et al. [135].

Hollow nanorices of ZnO have been used in the detection of toxic gases such as NO_2 and SO_2 [136]. ZnO core/shell hollow microspheres showed enhanced light harvesting in the quantum dots-sensitized solar cells [137]. Jeyabharathi et al. reported multi-sphere, highly porous ZnO micro and nanoparticles for biomedical applications [138]. Hollow zinc oxide microspheres prepared by a template-free hydrothermal method were reported for the photodegradation of organic dye [139].

However, these methods predominantly require the use of expensive chemicals, such as reducing agents, surfactants, or stabilizing agents. In addition, the synthesis processes are complex and involve multiple steps.

Sucrose is an inexpensive material that is widely available and requires no special storage conditions. In this study, sucrose-derived carbon was used as a template to synthesize ZHMSs, and the performance of this structure as a photocatalyst was evaluated. As crystallite size plays a major role in photocatalysis; thus, we prepared ZnO nanoparticles (ZNPs) of similar crystallite size to investigate the actual role of the hollow structure. To the best of our knowledge, a similar comparative study on hollow microspheres and non-hollow nanoparticles with identical crystallite sizes has not been previously reported.

Herein, we describe the synthesis, characterization, and photocatalytic application of ZHMSs and ZNPs of identical crystallite sizes to elucidate the role of hollow morphology on photocatalytic performance.

3.2 Experimental

3.2.1 Materials

Zinc nitrate hexahydrate, ($Zn(NO_3)_2 \cdot 6H_2O$, 98.0%) , sucrose, ($C_{12}H_{22}O_{11}$,99.5%), and polyvinylpyrrolidone (PVP, MW ~ 55,000) were purchased from Sigma-Aldrich (USA). Ethanol (99.5%) and Isopropanol (IPA, 99.7%) were obtained from KANTO CHEMICAL CO., INC. (Japan). Ethylenediaminetetraacetic acid (EDTA, 98%), catalase and p-benzoquinone (BQ, 97%) were supplied from TOKYO CHEMICAL INDUSTRY CO., LTD. Commercial TiO_2 (P25) was purchased from NIPPON AEROSIL (Japan).

3.2.2 Preparation of ZHMS

0.01 mol of $Zn(NO_3)_2 \cdot 6H_2O$ and 0.04 mol of sucrose were dissolved in 100 mL of deionized water. The solution was then transferred into 50-mL PTFE-lined stainless-steel autoclaves (three autoclaves were used) and heated at 180 °C for 16 h. The product was then washed multiple times with deionized water and ethanol. After washing, it was dried in an oven at 60 °C for 16 h followed by calcination at 600 °C for 4 h.

3.2.3 Preparation of ZNP

4 g $Zn(NO_3)_2 \cdot 6H_2O$ and 5 g PVP (Molecular weight ~ 55,000) were thoroughly dissolved in a 50:50 (v/v) mixture of deionized water and ethanol. The solution was heated at 80 °C for 1 h with constant stirring using a reflux system. The resulting gel was calcined at 650 °C for 4 h to obtain ZNP powder.

3.2.4 Characterizations

In this study, powder X-ray diffraction (XRD) patterns were recorded on a Rigaku Ultima IV diffractometer to determine the crystallinity of the ZHMSs and ZNPs in the 2θ range of 20–80° using Cu-K radiation (λ = 1.54056 nm). Field-emission scanning electron microscopy (FE-SEM; S-4500, Hitachi Ltd., Japan) and energy-dispersive X-ray spectrometry (EDX; S-782XII, Horiba Ltd., Japan) were employed to study the surface morphology and elemental composition. A Pt-Pd ion coating (E-1030, Hitachi Ltd., Japan) was used to sputter the samples prior to scanning electron microscopy (SEM) and SEM-EDX analyses. A PHI 5000 VersaProbe II X-ray photoelectron spectrometer (ULVAC-PHI Inc.) was used to study the surface chemical properties. Brunauer–Emmett–Teller (BET) surface area and pore size analyses were performed using a NOVA 1200e surface area and pore size analyzer. UV-vis diffuse reflectance spectroscopy (DRS) measurements were performed on a JASCO V-670 UV-vis spectrophotometer with an integrating sphere attachment of 60 mm.

3.2.5 Photocatalytic activity measurement

The photocatalytic activities of the ZHMSs and ZNPs were studied using RhB as the dye molecule. Initially, 2 mg of the ZHMS was dispersed in 20 mL of 10 ppm RhB solution, and the mixture was magnetically stirred for 30 min in the dark to ensure equilibrium adsorption on the catalyst surface. A 400-W Hg lamp, which produces light in the wavelength range of 254–577 nm with the highest intensity at 365 nm, was used to irradiate the sample solution with UV light. Next, approximately 1 mL of the RhB solution was extracted from the reaction tube, and the catalysts were then separated via centrifugation. The absorption of RhB was measured at 554 nm using a UV-vis spectrophotometer.

The photodegradation efficiency of the ZHMSs was calculated using the following equation [140]:

$$\% \text{ Degradation} = \frac{C_o - C}{C_o} \times 100$$

where C_o is the RhB concentration after equilibrium adsorption–desorption and C is the RhB concentration at different time intervals.

Finally, RhB degradation in the presence of the ZNPs was tested using a similar procedure.

3.2.6 Scavenging experiment

To identify the principal active species involved in the photodegradation of RhB, some specific scavengers were utilized. 2 mM isopropyl alcohol (IPA), 2 mM benzoquinone (BQ), 2 mM ethylenediamine tetraacetic acid (EDTA) and 100 units/mL catalase were introduced as the quencher for hydroxyl radical (•OH), superoxide anion radical ($\bullet O_2^-$), photogenerated hole (h^+) and H_2O_2, respectively [141]. The experimental conditions were similar to that of the photocatalytic experiment.

3.3 Results and discussions

The ZHMSs were prepared using a sucrose-assisted hydrothermal method. During the formation of the hollow structures, a core@shell composite was formed as a result of hydrothermal treatment (autoclaving) of $Zn(NO_3)_2 \cdot 6H_2O$ and sucrose at 180 °C for 16 h, followed by the decomposition of carbon core via calcination. Owing to the pressure that spontaneously developed within the autoclave system during the hydrothermal reaction, the sucrose dehydrated and carbonized. The hydrothermal decomposition of sugar yields carbonaceous spheres that are hydrophilic in nature and carry oxygen-containing functional groups such as –OH and C–O, which serve as anchors for metal ions [106].

The core@shell composite was formed due to the coordination or electrostatic interaction between the layers of adsorbed metallic ions on the carbon sphere. The calcination of solid materials at 600 °C led to the formation of several layers of dense ZnO nanocrystalline particles, while the carbon sphere was oxidized and decomposed concurrently. As a shape-directing agent, the surface of the carbon template plays a decisive role in forming ZnO hollow structures [107].

A sol–gel technique was used to synthesize the ZNPs. Due to high surface energy and surface area, almost all nanoparticles tend to aggregate. PVP was used as a surfactant to minimize the particle size and aggregation. PVP has also been reported to improve the surface morphology and microstructure [142].

XRD measurements were performed to determine the crystal structures, crystallite sizes, and phases of the ZHMS and ZNP photocatalysts. The XRD spectra of the ZHMSs and ZNPs are shown in Fig. 3.1. The XRD peaks of the ZHMS sample at 31.74°, 34.35°, 36.22°, 47.51°, 56.55°, 62.79°, 66.37°, 67.91°, 69.02°, 72.53°, and 76.91° can be assigned to the (100), (002), (101), (102), (110), (103), (200), (112), (201), (004), and (202) planes that aligned with hexagonal wurtzite ZnO (JCPDS 36-1451) [18]. In contrast, the XRD peaks of the ZNP sample at 31.75°, 34.40°, 36.23°, 47.51°, 56.56°, 62.83°, 66.34°, 67.93°, 69.08°, 72.55°, and 76.97° can be ascribed to the (100), (002), (101), (102), (110), (103), (200), (112), (201), (004), and (202) planes of ZnO (JCPDS 36-1451). These samples were highly crystalline and of high purity as no impurity peaks were detected. By applying the Debye–Scherer equation [143], the mean crystallite sizes of the ZHMSs and ZNPs were calculated to be 39.6 and 40.1 nm, respectively.

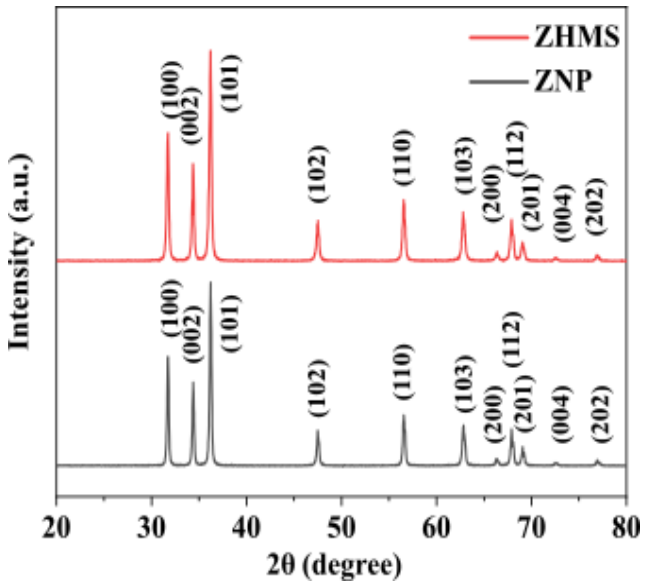

***Fig. 3. 1**: XRD spectra of the ZHMS and ZNP samples*

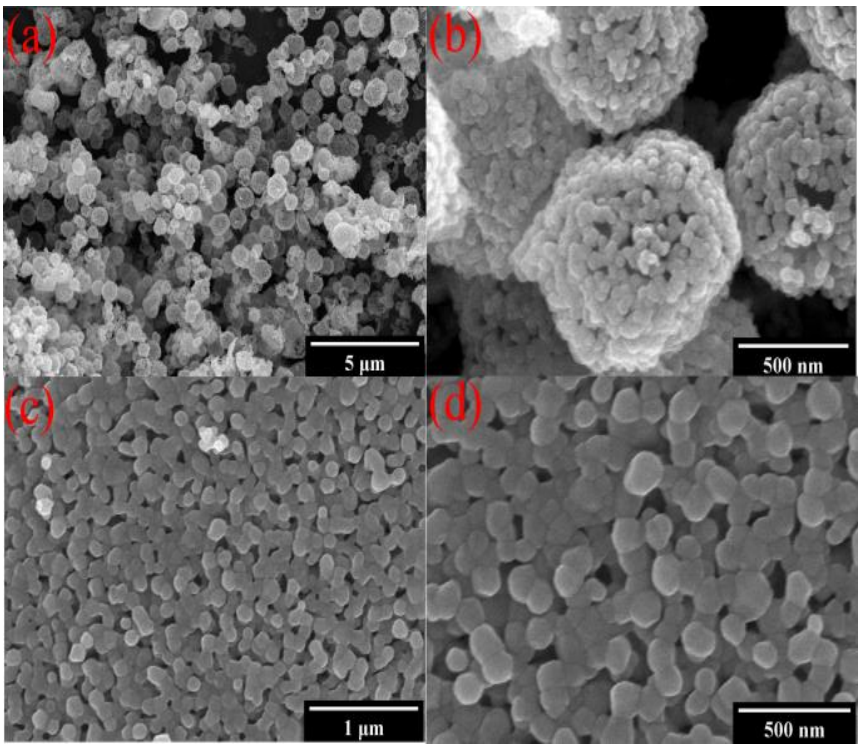

***Fig. 3. 2:** SEM images of the (a, b) ZHMSs and (c, d) ZNPs*

SEM was used to examine the morphological characteristics of the ZHMS and ZNP. Figs. 3.2a and 3.2b show the SEM images of the ZHMSs, demonstrating the aggregation of nanosized ZnO particles to create the shell of the hollow microspheres. In the SEM images, the shells of some microspheres appear thicker than those of others. These thicker shells were formed due to the deposition of multiple layers of ZNPs, resulting in both single- and multi-layered shells. In contrast, the SEM images of the ZNPs show the formation of spherical nanoparticles (Figs. 3. 2c and 3.2d).

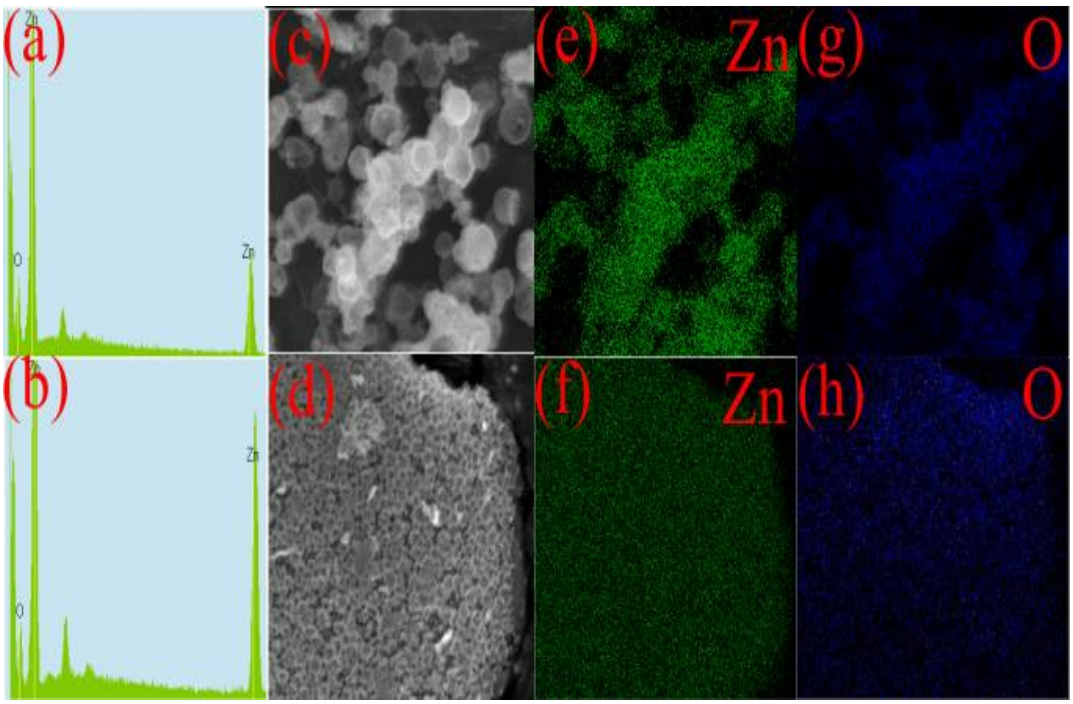

Fig. 3. 3: *Elemental distribution of the samples: EDX spectra of the (a) ZHMSs and (b) ZNPs, elemental mapping of the (c) ZHMSs and (d) ZNPs, Zn distribution in the (e) ZHMS and (f) ZNP samples, and O distribution in the (g) ZHMS and (h) ZNP samples*

EDX was employed to analyze the elemental compositions of the fabricated ZHMSs and ZNPs. Figs. 3.3a and 3.3b show the Zn and O peaks of the EDX spectra of the ZHMSs and ZNPs, respectively. Elemental mapping of the ZHMSs (Figs. 3.3c, 3.3e and 3.3g) was performed to observe the elemental distributions, which reveals that Zn and O covered the entire image frame and were homogeneously distributed within the ZHMS structure. Similar elemental mapping results were observed for the ZNPs (Figs. 3.3d, 3.3f and 3.3h). The corresponding mass and atomic percentages obtained from the EDX analysis are listed in Table 3.1.

Table 3. 1: *Elemental analyses of the ZHMS and ZNP*

Element	% Mass		% Atom	
	ZHMS	ZNP	ZHMS	ZNP
Zn	75.66	81.96	43.21	52.62
O	24.34	18.04	56.79	47.38
Total	100	100	100	100

The chemical states and elemental compositions of the ZHMS and ZNP were determined by X-ray photoelectron spectroscopy (XPS). Figs. 3.4a and 3.4b show the survey spectra of the ZHMSs and ZNPs, respectively. The XPS survey spectra of both samples exhibit peaks for Zn, O, and C, indicating the presence of Zn and O in the as-prepared ZHMS and ZNP photocatalysts. The C peak may have originated from the carbon tape used during the XPS measurements.

Both ZHMSs (Fig. 3.4c) and ZNPs (Fig. 3.4d) display two peaks at approximately 1022 and 1045 eV, respectively, in their Zn 2p spectra, which correspond to Zn $2p_{3/2}$ and Zn $2p_{1/2}$, respectively [76,144]. In addition, the difference between the doublet binding energies (~23 eV) indicates the existence of Zn as Zn^{2+} in the samples [144].

Fig. 3.4e and 3.4f depict the deconvoluted O 1s spectra of both samples, which show two peaks at binding energies of approximately 531 and 532 eV, respectively, corresponding to lattice oxygen and chemisorbed oxygen, respectively [76]. As shown in the O 1s spectra, the lower-energy peak was attributed to O^{2-} in the wurtzite structure, whereas the higher-energy peak was attributed to O^{2-} in oxygen-deficient ZnO [145]. A higher amount of O 1s, assigned to deficient O, indicates that •OH radicals were easily formed on the ZHMS sample.

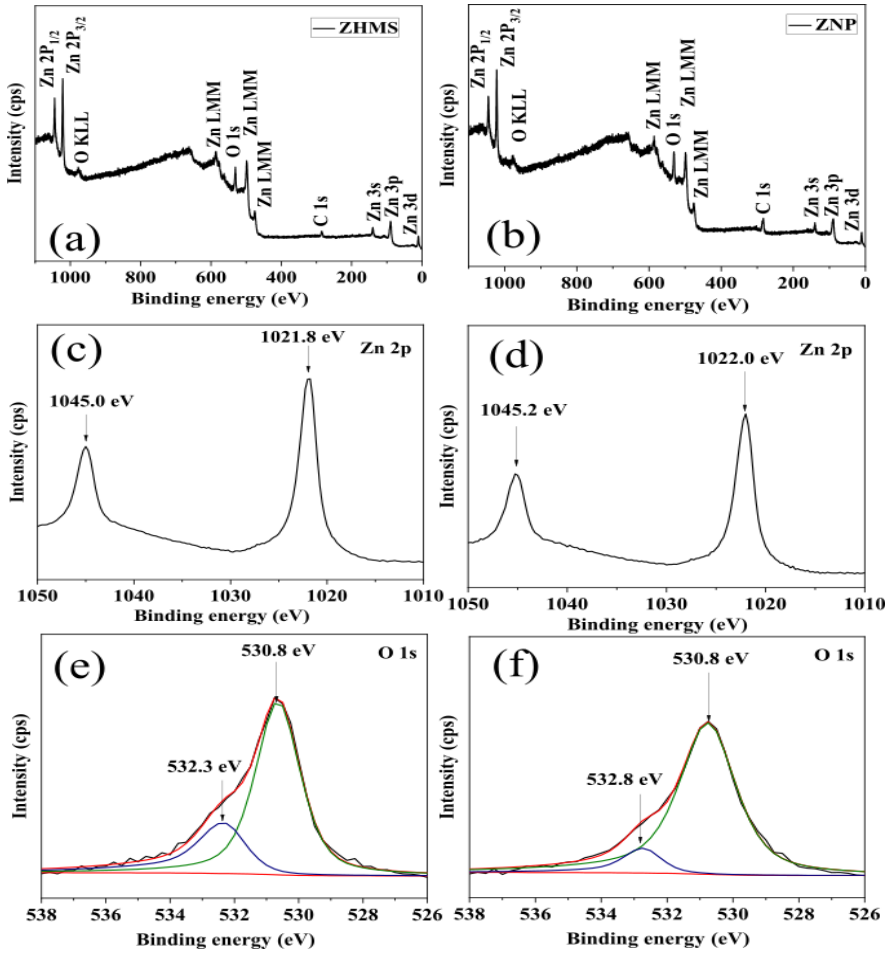

Fig. 3. 4: *XPS survey spectra of the (a) ZHMSs and (b) ZNPs, Zn 2p narrow spectra of the (c) ZHMSs and (d) ZNPs, and deconvoluted O 1s spectra of the (e) ZHMSs and (f) ZNPs*

Using BET analysis, the surface areas of the ZHMSs and ZNPs were found to be 7.73 and 4.61 m^2g^{-1}, respectively. The obtained isotherms (Figs. 3.5a and 3.5b) were classified as type III according to IUPAC [114]. The presence of a small hysteresis loop in the N_2 adsorption–desorption isotherms of both samples was an indication of capillary condensation, suggesting a mesoporous nature [115]. The graphs of differential volume vs. pore size of the ZHMSs (Fig. 3.5a (inset)) and ZNPs (Fig. 3.5b (inset)), obtained using the Barrett–Joyner–Halenda (BJH) pore-size analysis, show peaks at 3.58 and 3.6 nm, respectively. For the ZHMSs, macropores larger than 200 nm were detected, which may have contributed to the formation of hollow interiors. The mesopores in both ZHMSs and ZNPs may be derived from the intrapores between the ZNPs and pores within the ZNPs themselves.

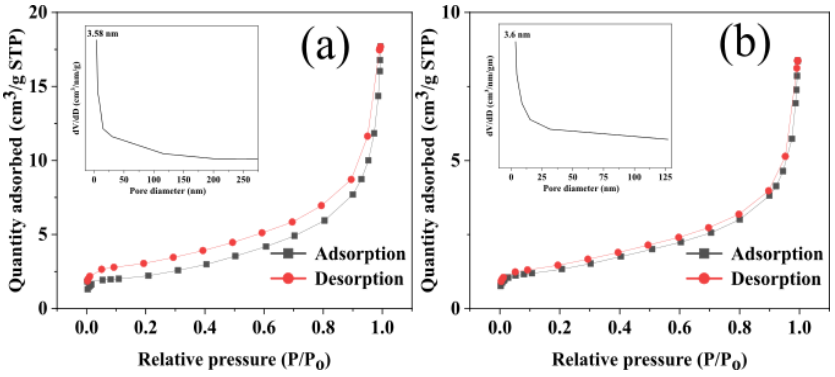

Fig. 3. 5: *Nitrogen adsorption–desorption isotherms of the (a) ZHMSs and (b) ZNPs. Insets show the graphs of differential volume vs. pore size constructed based on the BJH pore size distribution analysis*

The pore volumes of the ZHMSs and ZNPs were 0.025 and 0.011 ccg^{-1}, respectively. The surface area, pore size and pore volume of the prepared materials are analogous to that of other ZnO nanostructures reported in previous literature listed in Table 3.2.

Table 3. 2: *Comparison of BET surface areas of ZHMSs with previously reported literature*

Material	Morphology	Surface area (m^2g^{-1})	Pore size (nm)	Pore volume (cm^3g^{-1})	Reference
ZnO	Hollow microspheres	10.09	-	-	[146]
ZnO	Hollow microspheres	9.6	13.0	0.03	[147]
ZnO	Cauliflower-like structure	7.2	12.1	0.044	[148]
ZnO	Nanorods	3.3	3.92	-	[149]
ZnO	Hollow core/shell microspheres	10.02	-	-	[137]
ZnO	Nanoparticles	7.49	-	0.01	[150]
ZnO	Hollow microspheres	7.73	3.58	0.025	This work

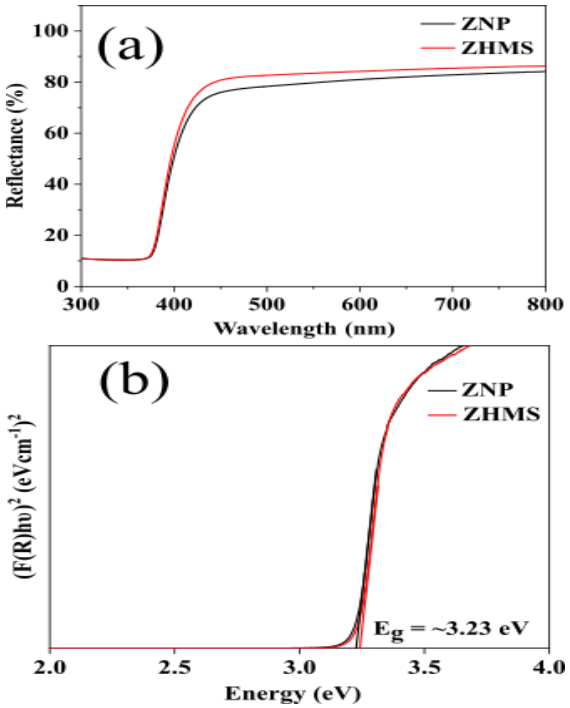

Fig. 3. 6: *(a) UV-vis DRS spectra and (b) Kubelka–Munk plots of the ZHMSs and ZNPs*

In addition to its large surface area, the ZHMS structure was found to enhance light scattering. Fig. 3.6a shows the UV-vis DRS spectra of the ZHMSs and ZNPs. Owing to the increased light reflection and scattering, ZHMSs can capture the light of different wavelengths for a longer duration.

From the Kubelka–Munk plot, the bandgaps of the prepared ZNPs and ZHMSs were calculated to be approximately 3.23 eV [151] in which no significant difference in the bandgap values was observed between the samples (Fig. 3.6b).

The photocatalytic activities of the ZHMSs and ZNPs were studied by monitoring RhB degradation. The reaction under ultraviolet irradiation was investigated, and the concentration of the dye molecules was measured using a UV-vis spectrophotometer. The intensity of the maximum absorption peak of RhB (554 nm) was monitored over time.

Figs. 3.7a and 3.7b show that the RhB absorbance gradually diminished over time in the presence of ZHMSs and ZNPs, respectively. The RhB concentration was calculated from the absorbance values by applying the Beer–Lambert law [152] It was found that after 90 min of UV irradiation, the RhB concentration decreased by approximately 95 % and 85 % in the presence of ZHMSs and ZNPs, respectively. Although ZNPs exhibited lower photocatalytic performance than commercial TiO_2, ZHMSs performed better than TiO_2 as a photocatalyst. The photocatalytic efficiency of ZHMSs was also compared with the ZnO photocatalysts with varied morphologies from the previous studies and results are displayed in Table 3.3.

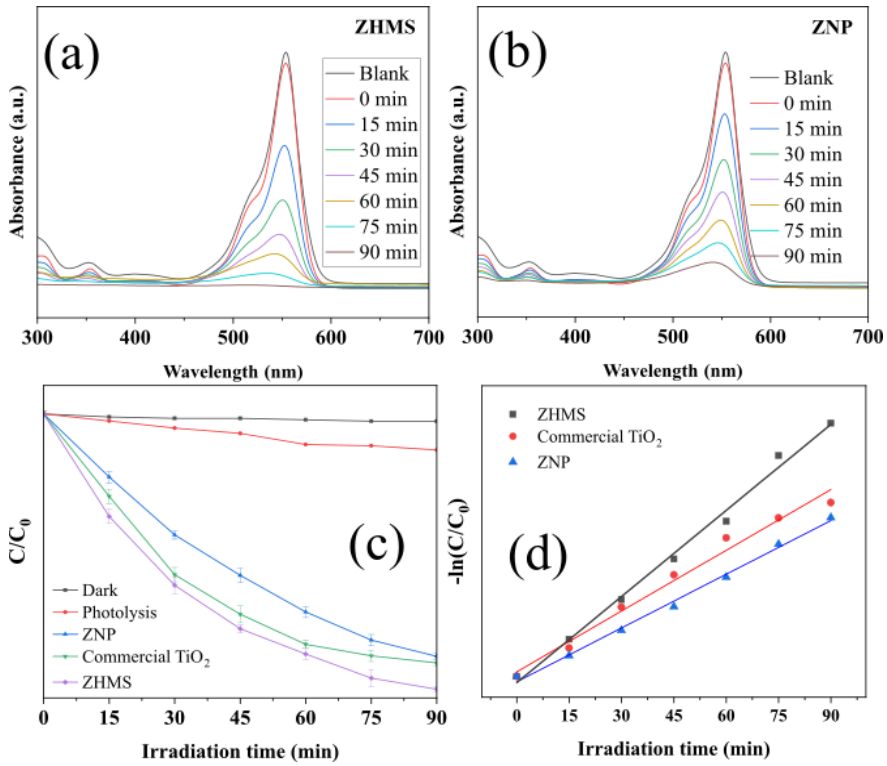

Fig. 3. 7: *Time-dependent UV-vis absorbance spectra of the RhB aqueous solution treated with the (a) ZHMSs and (b) ZNPs; plots of (c) photocatalytic degradation and (d) first-order reaction kinetics*

Additionally, the C/C_0 plots of the RhB photodegradation can determine which is the optimal ZnO structure for photocatalysis (Fig. 3.7c). The photodegradation kinetics of RhB can be defined as $-\ln(C/C_0) = kt$, where k is the first-order kinetic constant and t is the irradiation time (Fig. 3.7d). For RhB degradation in the presence of ZHMSs and ZNPs, the R^2 value was found to be > 0.99. The k value for the ZHMSs (0.03456 min^{-1}) was larger than that of the ZNPs (0.02157 min^{-1}), indicating the superior efficiency of the ZHMSs towards photodegradation.

No significant photodegradation was observed in dark, but a considerable 12% of RhB was degraded during photolysis.

Table 3. 3: *Comparison of photodegradation efficiency of ZHMSs with other ZnO photocatalysts reported against different dye molecules*

Photocatalyst	Pollutant	Concentration	Catalyst loading	Light source	Irradiation time	Photodegradation (%)	Reference
ZnO hollow spindles	Rhodamine blue	0.02 mM	10 mg	UV	120 min	23	[153]
ZnO hollow spheres	Crystal violet	-	0.5 g	UV	75 min	79.5	[154]
ZnO hollow microflower	Rhodamine blue	15 ppm	0.05 g	UV	80 min	80	[155]
ZnO nanoparticles	Methylene blue	10 ppm	100 mg	UV	180 min	90.5	[156]
ZnO nanoparticles	Red S3B	50 ppm	100 mg	UV	120 min	80	[157]
ZnO nanoparticles	Congo red	100 ppm	100 mg	UV	180 min	93	[158]
ZnO nanoparticles	Congo red	30 ppm	100 mg	UV	240 min	62	[159]
ZnO hollow microspheres	Rhodamine blue	10 ppm	2 mg	UV	90 min	95	This work

This higher photocatalytic efficiency can be attributed to the nanoporous structure of the ZHMSs, which allows for more efficient transportation to the active sites of the reagent molecules, thus increasing the photocatalytic efficiency.

The light reflection and scattering properties appear to contribute very little to the high photocatalytic activity of the ZHMSs owing to their large bandgap. Using the Planck equation, the wavelength corresponding to the bandgap energy (3.23 eV) was calculated to be 384 nm [160]. Based on the UV-vis DRS spectra, light absorption, which is responsible for the transfer of electrons from the valence band to the conduction band, occurs primarily below 384 nm, while light scattering occurs above 384 nm.

Because the bandgaps of the ZHMSs and ZNPs are similar, they are both restricted to absorbing light of higher wavelengths, that is, > 384 nm. In addition, light after reflection and scattering possesses lower energy, which may not contribute to photocatalysis. Therefore, higher light scattering properties have little or no contribution to the photocatalytic performance of the ZHMSs.

A photocatalytic mechanism (Fig. 3.8) was hypothesized by dissolving a variety of trapping agents in solution and determining the main photoactive species during the photodegradation process.

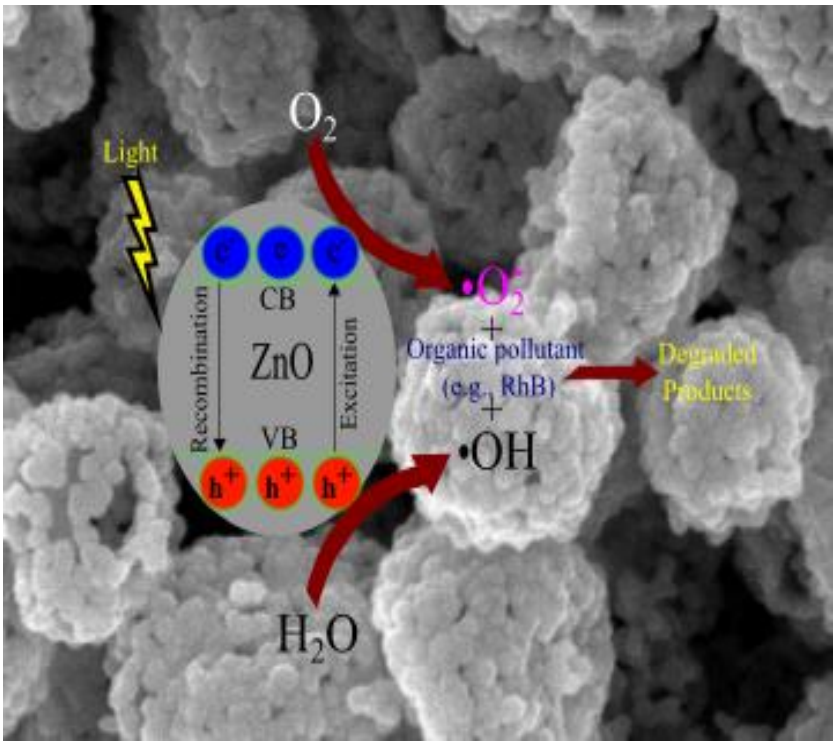

Fig. 3. 8: *Schematic diagram illustrating the possible photocatalytic mechanism in ZHMSs for RhB degradation*

EDTA, BQ, IPA and catalase were used to eliminate the h^+, $\bullet O_2^-$, •OH and H_2O_2, respectively. From the scavenger experiment, it is evident that photogenerated holes and superoxide radicals are the dominant reactive oxygen species (ROS). Also, •OH radical trapping in ZHMSs showed a considerable reduction in degradation efficiency (Fig. 3.9a). Therefore, more •OH radicals are formed in the ZHMSs. However, their formation mechanism is yet unknown.

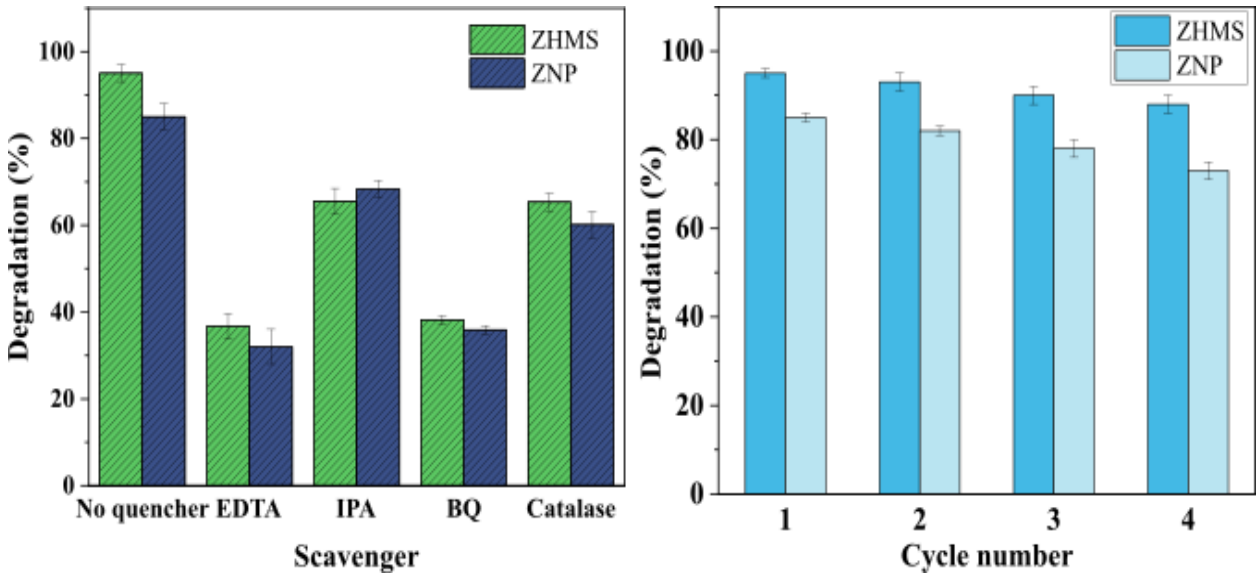

Fig. 3. 9: *(a) Radical trapping assessment of reactive oxygen species during RhB photodegradation over ZHMSs and ZNPs, and (b) photodegradation of RhB using ZHMSs and ZNPs over four cyclic runs*

When radiation hits the ZnO photocatalyst surface with energy (hυ) equal to or higher than the bandgap of the catalyst, electrons (e^-) initially at the valence band (VB) gain energy and transfer to the conduction band (CB) by leaving holes (h^+) at VB. These photo-generated holes react with the chemisorbed water molecules which lead to the formation of hydroxyl radicals (OH•) and protons (H^+).

On the other hand, photo-generated electrons in the ZnO conduction band (CB) react with oxygen molecules and generate superoxide radicals ($\bullet O_2^-$). [161]. These radicals react with electrons and protons to yield H_2O_2. Photogenerated holes themselves can take part in the photodegradation or produce more hydroxyl radicals (OH•). The photocatalytic mechanism can be proposed as follows [162–165]

$$ZnO + h\upsilon \rightarrow ZnO\ (h^+ + e^-) \quad (1)$$

$$e^- + O_2 \rightarrow \bullet O_2^- \quad (2)$$

$$h^+ + H_2O \rightarrow OH\bullet + H^+ \quad (3)$$

$$\bullet O_2^- + e^- + 2H^+ \rightarrow H_2O_2 \quad (4)$$

$$h^+ + \text{dye} \rightarrow \text{degradation products} \quad (5)$$

$$OH\bullet + \text{dye} \rightarrow \text{degradation products} \quad (6)$$

$$\bullet O_2^- + \text{dye} \rightarrow \text{degradation products} \quad (7)$$

$$H_2O_2 + \text{dye} \rightarrow \text{degradation products} \quad (8)$$

The feasibility of photodegradation efficiency was also examined with a recycling test (Fig. 3.9b). The performance of ZHMSs and ZNPs was studied in four consecutive runs of RhB photodegradation under UV-light irradiation. The ZHMSs and ZNPs were collected after each run, dried, and reused under the same experimental conditions. After four cycles, ZHMSs and ZNPs exhibited a 7% and 15% loss in degradation efficiency, respectively. Therefore, both photocatalysts are stable and reusable for long-term practical photocatalytic applications.

In ZHMSs, nanoparticles aggregate to form the shell which puts more weight on the material. As a result, separation from slurry becomes easier for ZHMSs leading to better performance in the reusability test.

3.4 Conclusions

A facile hydrothermal technique was used in this study to fabricate ZHMSs. To study the role of the hollow morphology of the ZHMSs, ZNPs of similar crystallite sizes were fabricated by a sol–gel method, in which the crystallite size was controlled using a specified amount of PVP. The FE-SEM images showed that the resulting ZHMS samples had hollow interiors, and hollow microspheres were formed by the deposition of zinc ions on a sucrose-derived carbon core, followed by the decomposition of the core via calcination. EDX spectra of the ZHMSs and ZNPs showed signals of Zn and O. The fabricated ZHMS and ZNP photocatalysts were used to degrade RhB dye under UV light. The ultraviolet light responsive and optimized ZHMSs demonstrated higher degradation efficiency (~95%) towards the RhB dye compared to the ZNPs (~85%). Moreover, the ZHMS and ZNP photocatalysts exhibited first-order kinetics with rate constants of 0.03456 min^{-1} and 0.02157 min^{-1}, respectively. Therefore, the ZHMSs can be used for the treatment of dyes and organic contaminants from both polluted water and wastewater at a commercial level owing to their ability to respond to ultraviolet light.

CHAPTER 4

Facile one-pot hydrothermal synthesis of hollow ZnO/$ZnFe_2O_4$ composite microspheres with an ultrahigh surface area

Abstract

This work represents the synthesis of hollow ZnO/$ZnFe_2O_4$ microspheres by a one-pot hydrothermal technique. Sucrose-assisted synthesis of these composites has been reported for the first time in this study. The hybrid hollow composites are composed of well-dispersed ZnO and $ZnFe_2O_4$ nanoparticles. The crystalline phase, surface morphology, and elemental composition of the prepared composite were characterized by X-ray diffraction, field-emission scanning electron microscopy, energy-dispersive X-ray spectroscopy, and X-ray photoelectron spectroscopy. BET surface area for this material was calculated to be 1051 m^2g^{-1}, which is the highest value for this hollow composite material according to our known literature.

4.1 Introduction

In recent years, hollow nanomaterials with remarkable interior void spaces have received extensive research due to their nanostructured walls, low density, higher surface area to volume ratio, and high permeability for controlled mass transport [166,167]. ZnO/$ZnFe_2O_4$ composite has been investigated for many applications, such as lithium-ion battery [168], gas sensing [22,169–171], photocatalysis [172–174] and colourimetric biosensing [175]. Certain drawbacks of pure ZnO such as inferior selectivity towards gases and poor visible light absorption could be resolved by doping it with $ZnFe_2O_4$.

Compared to other p-type semiconductors, $ZnFe_2O_4$ has a narrow band gap (1.96 eV), outstanding photochemical stability, environmental friendliness, good sensitivity and selectivity to gases, low cost, and high thermal and chemical stability [22,166]. Due to its low activation energy, the $ZnFe_2O_4$ is capable of sensing reducing gases efficiently [23]. Moreover, the incorporation of $ZnFe_2O_4$ into ZnO is effective in controlling their optical properties [176].

On the other hand, due to the easy aggregation of pure ZnO, absorption and reaction are limited to a small part of the material. This problem can be dealt with by creating a hollow structured composite. A hollow structure also comes with an increased specific surface area.
As reactions predominantly take place on the surface of the materials, a high surface area could offer an ample "reaction field" for gas adsorption and identification [22].

Various types of techniques have been used to fabricate $ZnO/ZnFe_2O_4$ hollow composite materials e.g., hydrothermal [22], solvothermal [177], electrospinning [23], chemical precipitation [174], atomic layer deposition (ALD) [178], microwave-assisted heating [179], and impregnating–calcination process [166]. Qin et al. prepared nanostructured $ZnO\text{-}ZnFe_2O_4$ heterojunction by thermal decomposition of metal–surfactant complexes for photoelectrochemical water oxidation [180]. $ZnO\text{-}ZnFe_2O_4$ hollow nanofiber was fabricated for the H_2S gas sensor using a one-needle syringe electrospinning method [23]. A surfactant-free solvothermal process was used to prepare octahedral $ZnO/ZnFe_2O_4$ heterostructure for malachite green adsorption [177]. Janus hollow nanofibers of $ZnO/ZnFe_2O_4$ were investigated for photocatalytic degradation of organic dyes [178].

In this study, the $ZnO/ZnFe_2O_4$ hollow microsphere with an ultra-high surface area was fabricated by a carbon template-assisted hydrothermal method. As high surface area is the key requirement for boosted surface reactions, this material could be highly useful in different surface-related applications.

4.2 Experimental

4.2.1 Materials

Zinc nitrate hexahydrate, ($Zn(NO_3)_2 \cdot 6H_2O$, 98.0%) and sucrose, ($C_{12}H_{22}O_{11}$, 99.5%) were purchased from Sigma-Aldrich (USA). Ferric chloride anhydrous ($FeCl_3$, 96.0%) was procured from Kanto Chemical Co. Inc. (Japan). All chemicals were analytically pure and were used in the experiment without further purification.

4.2.2 Preparation of $ZnO/ZnFe_2O_4$ hollow microspheres

First, $Zn(NO_3)_2.6H_2O$, anhydrous $FeCl_3$ and sucrose were dissolved in deionized water. Then, the solution was sealed in a 100 mL capacity Teflon-lined stainless-steel autoclave and heated at 180^{o}C for 16h. After washing with deionized water and ethanol, the product was dried in an oven. The dried product was then calcined in air at 500^{o}C for 6h to get the desired product.

4.2.3 Characterizations

In this study, X-ray diffraction (XRD) patterns were obtained using a Rigaku Ultima IV diffractometer. To study the surface morphology and elemental composition, field-emission scanning electron microscopy (FE-SEM; S-4500, Hitachi Ltd., Japan) and energy-dispersive X-ray spectrometry (EDX; S-782XII, Horiba Ltd., Japan) were employed.

A PHI 5000 VersaProbe II X-ray photoelectron spectrometer (ULVAC-PHI Inc.) was used to study the surface chemical properties. Brunauer–Emmett–Teller (BET) surface area and pore size analyses were performed in a NOVA 1200e surface area and pore size analyzer.

4.3 Results and discussions

The template-assisted synthesis of hollow structured microspheres utilizing sucrose generally involves the adsorption of metal ions on the surface of carbon microspheres, and subsequent removal of carbon via calcination (Fig. 4.1). Through a hydrothermal reaction, sucrose can efficiently produce carbonaceous spheres with a hydrophilic surface [181]. The metallic ions (e.g., Zn^{2+} and Fe^{3+}) get adsorbed onto the surface of carbonaceous spheres to form core@shell composites.

A complicated process takes place during the heating of the $ZnFe_2O_4$ precursor. At lower temperatures, bound water is eliminated, and precursors are converted to ZnO and Fe_2O_3. A high temperature during the heating process causes carbon microspheres to decompose and $ZnFe_2O_4$ to form from the reaction of ZnO and Fe_2O_3 [166].

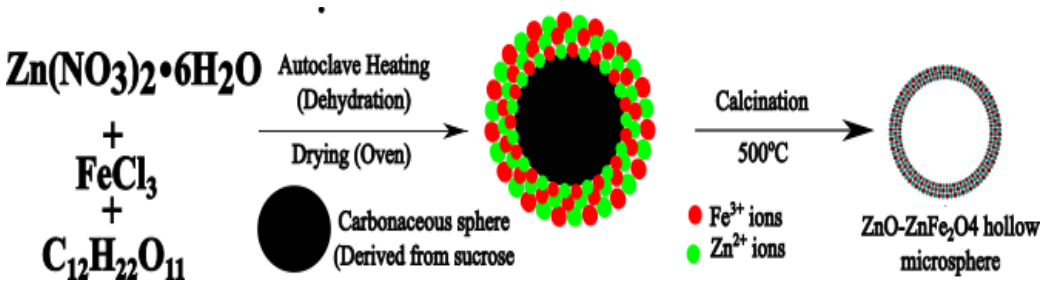

Fig. 4. 1: *Schematic representation of the possible synthetic mechanism of ZnO/$ZnFe_2O_4$ hollow composite microspheres*

To determine the phase of the composite, XRD analysis was used (Fig. 4.2). The peaks at 31.76°, 34.39°, 36.26°, 47.58°, 62.86°, 67.93° are considered to be the characteristic peaks of the ZnO wurtzite structure (JCPDS no. 36-1451) [144]. Peaks at 18.04°, 29.93°,35.15°, 42.72°, 53.02°, 56.58°, 62.27°, and 73.40° correspond to the cubic phase of $ZnFe_2O_4$ [166].

As diffraction peaks of Fe-related phases such as α-Fe_2O_3, γ-Fe_2O_3, FeO, and Fe_3O_4 were not spotted in the XRD pattern, it can be confirmed that the obtained composite consists of $ZnFe_2O_4$ and ZnO phases.

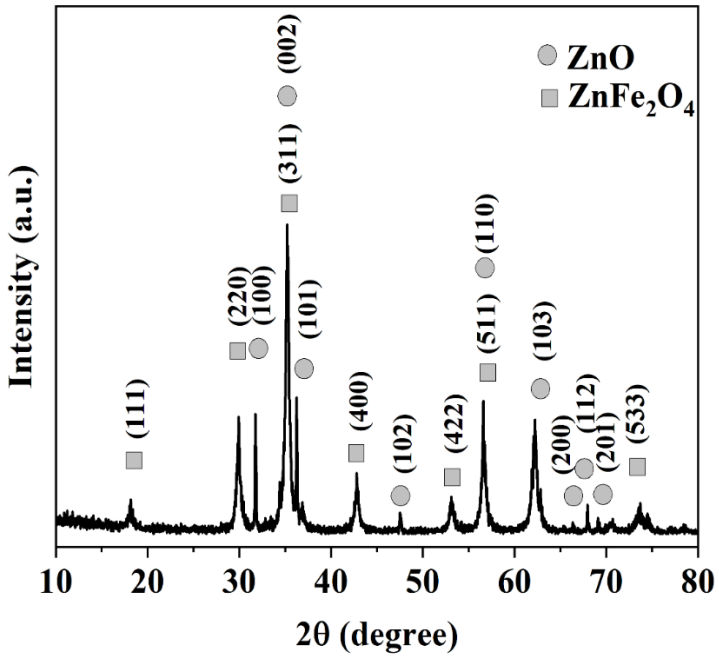

Fig. 4. 2: *XRD spectra of ZnO/$ZnFe_2O_4$ hollow composite microspheres*

SEM images of hollow microspheres containing ZnO/$ZnFe_2O_4$ are shown in Figure 4.3(a-d). It appears from the images that the surface of the hollow microspheres is rough, coarse, and broken. There were some hollow spheres (Fig. 4.3(b-d)) with openings, which might be the result of template removal. The microsphere size ranges from 500 nm to 2.5 μm.

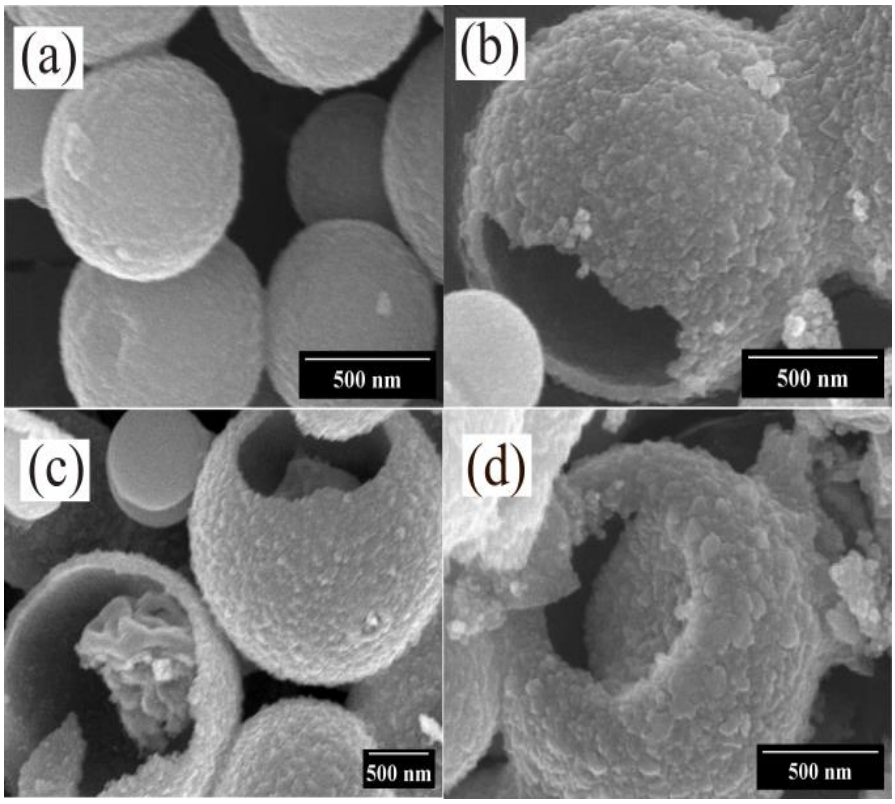

Fig. 4. 3: *SEM images of $ZnO/ZnFe_2O_4$ hollow composite microspheres*

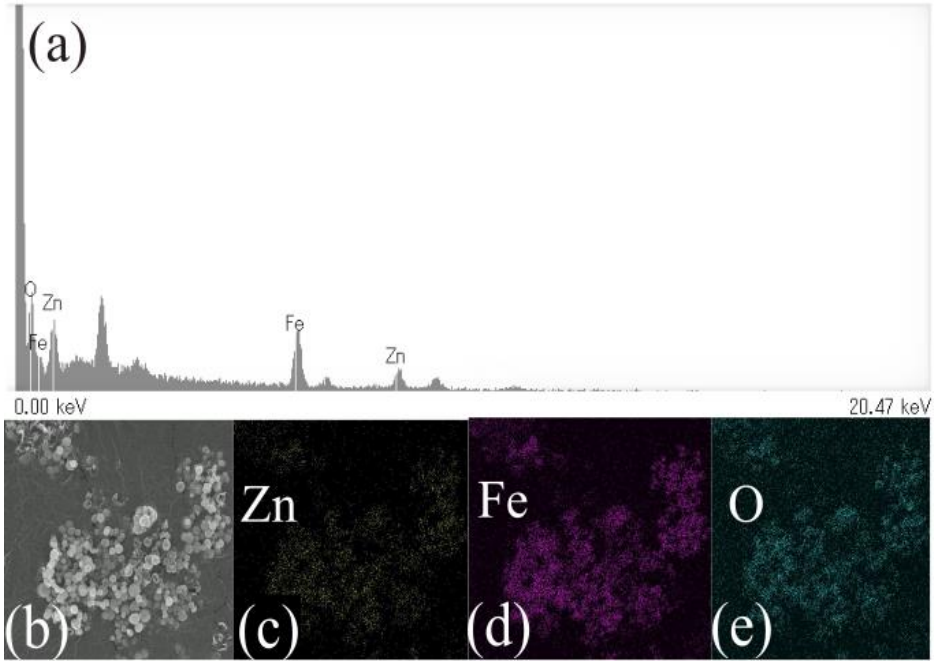

Fig. 4. 4: *Elemental distribution of $ZnO/ZnFe_2O_4$ hollow composite microspheres: (a) EDX spectra (b) elemental mapping; distribution of elements (c) Zn (d) Fe and (e) O*

EDX study of $ZnO/ZnFe_2O_4$ verified the Zn, Fe and O elements. The elements covered the entire image frame and were evenly distributed throughout the $ZnO/ZnFe_2O_4$ structure. Table 4.1 displays the corresponding atomic and mass percentages of the elements.

Table 4. 1: *Elemental analyses of $ZnO/ZnFe_2O_4$ hollow composite microspheres*

Element	%Mass	%Atom
O	37.66	69.28
Fe	34.49	18.18
Zn	27.85	12.54
Total	100	100

To analyze the surface chemical composition of different elements and their atomic states, XPS analysis was carried out. Fig. 4.5a shows elemental signals of the $ZnO/ZnFe_2O_4$.
Fig. 4.5b indicates that Zn $2p_{1/2}$ and Zn $2p_{3/2}$ have two peaks at 1045.0 and 1021.8 eV, respectively suggesting the +2 chemical state of Zn and the existence of Fe-containing component in the composite [23,170,182].

To fit the XPS spectra of Fe 2p, the spin-orbit doublets were considered (Fig. 4.5c). Peaks at 711.0 and 713.2 eV represent Fe $2p_{3/2}$ tetrahedral and octahedral structures, respectively. The peak at 719.5 eV was consistent with Fe $2p_{1/2}$, while at 725.2 eV, the peak can be attributed to the shake-up satellite structure indicating the normal state of Fe^{3+} in the resulting composite [178].

Gaussian-Lorentzian functions were used to fit O 1s (Fig. 4.5d). A peak at 530.0 eV can be attributed to surface lattice oxygen (O^{2-}) oxygen, whereas the other peak at 532.2 eV indicates surface adsorbed oxygen (O^{-} and O_2^{-}) [22].

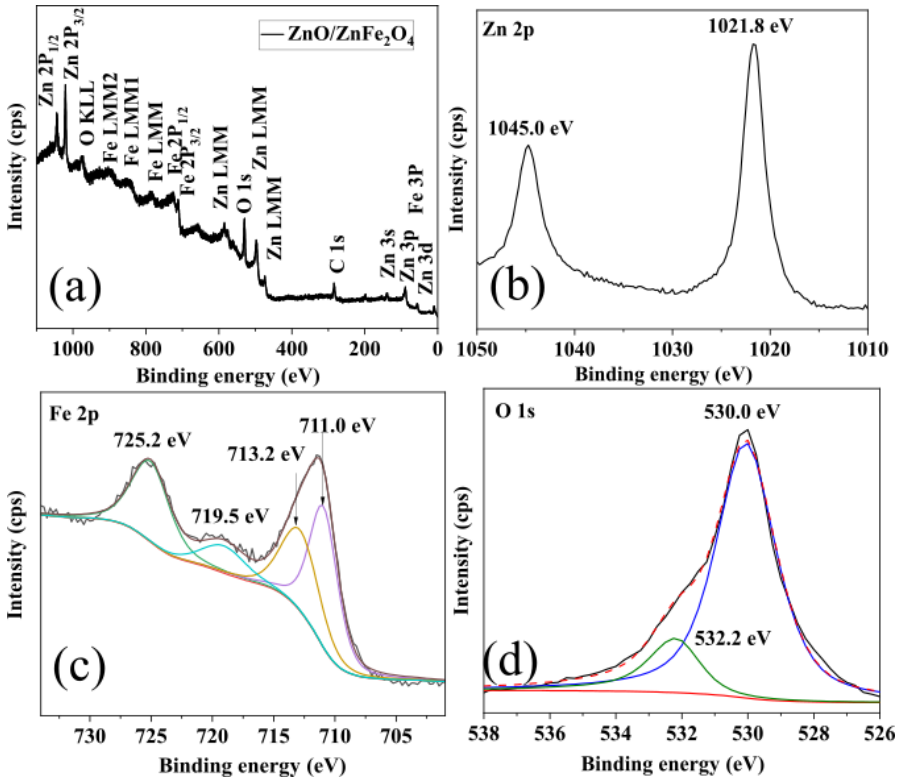

Fig. 4. 5: *XPS spectra of ZnO/ZnFe₂O₄ hollow composite microspheres: (a) survey spectra (b) Zn 2p narrow spectra (c) deconvoluted Fe 2p and (d) deconvoluted O 1s spectra*

The surface area of the prepared composite was obtained by nitrogen adsorption-desorption isotherms measurement (Fig. 4.6). Based on the IUPAC classification, this isotherm is type IV and representative of mesoporous materials [114]. The surface area of the hollow composite microspheres was found to be 1051 m^2g^{-1}.

Average pore size and pore volume were calculated to be 15.6 nm and 3.977 cc/g, respectively using Barrett-Joyner-Halenda (BJH) method (Fig. 4.6(inset)). The surface area of this material was compared with the previously reported studies which are shown in Table 4.2.

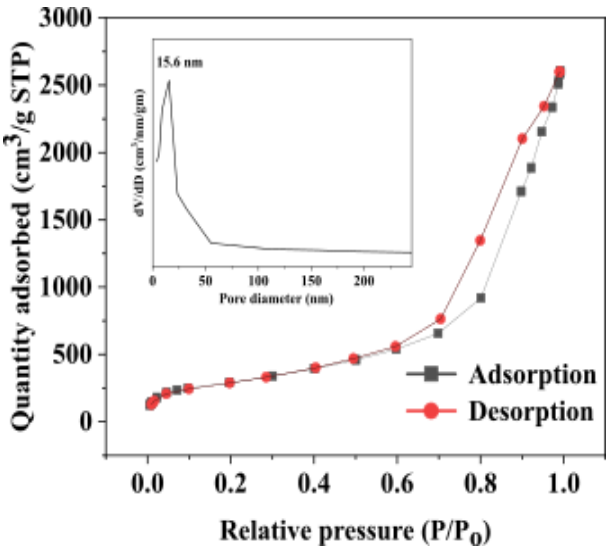

Fig. 4. 6: *Nitrogen adsorption-desorption isotherms of $ZnO/ZnFe_2O_4$ hollow composite microspheres. Inset represents the graph of differential volume vs. pore size obtained from BJH pore size distribution analysis*

Table 4. 2: *Comparison of surface areas of the composite with previously reported literature*

Material	Morphology	Method	Surface area (m^2g^{-1})	Pore size (nm)	Pore volume ($cm^3 \cdot g^{-1}$)	Reference
$ZnO/ZnFe_2O_4$	Hollow cubes	Pyrolysis	50	8	-	[170]
$ZnO/ZnFe_2O_4$	Core-shell	Hydrothermal	67	-	-	[182]
$ZnO/ZnFe_2O_4$	Octahedral	Solvothermal	60.45		0.94	[177]
$ZnFe_2O_4$@ZnO	Core-shell	Microwave-assisted	41	7.5	4.6×10^{-2}	[172]
$ZnFe_2O_4$/ZnO	Hollow spheres	Hydrothermal	30.8	9.12	-	[171]
ZnO/ZnFe2O4	Nanoparticles	Microwave combustion	94.466	-	-	[183]
$ZnO/ZnFe_2O_4$	Hollow microsphere	Hydrothermal	1051	15.6	3.977	This work

4.4 Conclusions

Sucrose assisted one-pot hydrothermal method for the fabrication of hollow $ZnO/ZnFe_2O_4$ has been reported for the first time. The prepared hollow composite has been analyzed by different characterization techniques. A massive surface area, pore size and pore volume were recorded for this material, which can contribute to faster surface reactions in different surface-related applications. The synthesis procedure is quite simple and can be adapted for the fabrication of other binary/ternary hollow composite materials.

CHAPTER 5

Discussions and Future Research

In this research work, hollow structured nanomaterials and nanocomposites have been fabricated by a simple, cost-effective, one-pot hydrothermal technique. As the unique characteristics of the hollow structure confer many benefits, such as discrete cavities, large specific surface area, abundant pores, high structural stability, spatial confinement effect, high product selectivity, short electron transport distance etc., research has progressed significantly in various fields as a result of these advantages.

However, many challenges remain in the synthesis of hollow structured micro/nanomaterials despite their successful synthesis with diverse compositions and morphologies. The first issue is that few hollow structures can be synthesized in large quantities by specific methods, which is far from being sufficient for actual production.

One of the most important factors limiting the commercial application of hollow structural materials is their yield. In addition, most of the mechanism underlying hollow structure formation is still a matter of speculation, without more direct evidence. It is necessary to introduce some advanced technologies and concepts to meet these challenges.

Future research on hollow structured materials should consider the following aspects:

i. Hollow structured materials are restricted by their yield, which is one of the main factors preventing their large-scale use. Therefore, mass production of these materials must be studied to make them a useful in practical industrial production. However, heat and mass transfer between small and large chemical reaction systems differ significantly. Larger systems have more difficulty transferring heat and mass, which results in poor homogeneity. The advancement of computer simulation technology has brought good news to it. To simulate laboratory conditions as closely as possible, mass and heat transfer can be scaled up through computer simulations. It is also feasible to optimize the synthesis process and develop new synthesis techniques for hollow structures.

ii. Most of the mechanisms responsible for hollow structure formation are still in the stage of speculation or ex-situ observations at present. A direct in situ observation of hollow structures can be achieved using in situ electron microscopy or in situ liquid infrared, to better understand their synthesis mechanisms. By using in situ electron microscopy, hollow structures can be observed during their nucleation and crystallization. During crystallization and nucleation of hollow structures, in situ infrared may provide insights into reactant molecules' behavior.

iii. Multi-shell porous hollow structures constructed by nano-units with exposed crystal planes may be more useful for research and development.

In addition to maximizing space and increasing the effective surface area, multi-shell hollow structures are also capable of regulating the transport of substances through layer spacing, layer thickness, and pore channels [184]. The specific crystal plane nano-units, on the other hand, can expose the active crystal plane more easily, improving catalytic activity [185]. Thus, the combination of these two approaches may be one of the research directions of hollow structures in the future.

To conclude, there is still a lot of work to be done to fully harness the potential of hollow structured materials for real-life applications.

References

[1] R.T.M. Situmeang, R.T.M. Situmeang, Preparation of Hollow Nanostructures via Various Methods and Their Applications, Nov. Nanomater. (2021). https://doi.org/10.5772/INTECHOPEN.95272.

[2] L. Fang, Y. Xie, Y. Yang, B. Zhu, Y. Wang, M. Liu, K. Zhao, H. Zhao, J. Zhang, Interfacial Electronic Modulation of Multishelled CoP Hollow Spheres via Surface Reconstruction for High-Efficient Hydrogen Evolution Reaction, ACS Appl. Energy Mater. 3 (2020) 309–318. https://doi.org/10.1021/ACSAEM.9B01562.

[3] X. Yu, J. Wu, A. Zhang, L. Xue, Q. Wang, X. Tian, S. Shan, C.J. Zhong, S. Zeng, Hollow copper–ceria microspheres with single and multiple shells for preferential CO oxidation, CrystEngComm. 21 (2019) 3619–3626. https://doi.org/10.1039/C9CE00272C.

[4] S. Zhang, Q. Fan, H. Gao, Y. Huang, X. Liu, J. Li, X. Xu, X. Wang, Retracted Article: Formation of Fe_3O_4@MnO_2 ball-in-ball hollow spheres as a high performance catalyst with enhanced catalytic performances, J. Mater. Chem. A. 4 (2016) 1414–1422. https://doi.org/10.1039/C5TA08400H.

[5] S. Xiong, H.C. Zeng, Serial Ionic Exchange for the Synthesis of Multishelled Copper Sulfide Hollow Spheres, Angew. Chemie Int. Ed. 51 (2012) 949–952. https://doi.org/10.1002/ANIE.201106826.

[6] J. Zhang, Y. Cao, C.A. Wang, R. Ran, Design and Preparation of MnO_2/CeO_2-MnO_2 Double-Shelled Binary Oxide Hollow Spheres and Their Application in CO Oxidation, ACS Appl. Mater. Interfaces. 8 (2016) 8670–8677. https://doi.org/10.1021/ACSAMI.6B00002.

[7] X. Qian, W. Wu, Y. Niu, J. Yang, C. Xu, K.Y. Wong, Triple-Shelled Co-VSe_x Hollow Nanocages as Superior Bifunctional Electrode Materials for Efficient Pt-Free Dye-Sensitized Solar Cells and Hydrogen Evolution Reactions, ACS Appl. Mater. Interfaces. 11 (2019) 43278–43286. https://doi.org/10.1021/ACSAMI.9B16623.

[8] Z.W. Shan, G. Adesso, A. Cabot, M.P. Sherburne, S.A. Syed Asif, O.L. Warren, D.C. Chrzan, A.M. Minor, A.P. Alivisatos, Ultrahigh stress and strain in hierarchically structured hollow nanoparticles, Nat. Mater. 7 (2008) 947–952. https://doi.org/10.1038/nmat2295.

[9] Y. Du, M. Zhang, Z. Wang, Y. Liu, Y. Liu, Y. Geng, L. Wang, A self-templating method for metal–organic frameworks to construct multi-shelled bimetallic phosphide hollow microspheres as highly efficient electrocatalysts for hydrogen evolution reaction, J. Mater. Chem. A. 7 (2019) 8602–8608. https://doi.org/10.1039/C9TA00557A.

[10] B. Nowack, T.D. Bucheli, Occurrence, behavior and effects of nanoparticles in the environment, Environ. Pollut. 150 (2007) 5–22. https://doi.org/10.1016/J.ENVPOL.2007.06.006.

[11] H.P.S. Abdul Khalil, R. Dungani, M.S. Hossain, N.L.M. Suraya, S. Aprilia, A.A. Astimar, Z. Nahrul Hayawin, Y. Davoudpour, Mechanical properties of oil palm biocomposites enhanced with micro to nanobiofillers, Biocomposites Des. Mech. Perform. (2015) 401–435. https://doi.org/10.1016/B978-1-78242-373-7.00026-3.

[12] Nanomaterials definition matters, Nat. Nanotechnol. 14 (2019) 193–193. https://doi.org/10.1038/s41565-019-0412-3.

[13] I. Neitzel, V. Mochalin, Y. Gogotsi, Advances in Surface Chemistry of Nanodiamond and Nanodiamond–Polymer Composites, Ultrananocrystalline Diam. Second Ed. (2012) 421–456. https://doi.org/10.1016/B978-1-4377-3465-2.00013-X.

[14] A.S. Teja, P.Y. Koh, Synthesis, properties, and applications of magnetic iron oxide nanoparticles, Prog. Cryst. Growth Charact. Mater. 55 (2009) 22–45. https://doi.org/10.1016/J.PCRYSGROW.2008.08.003.

[15] M. Tadic, L. Kopanja, M. Panjan, J. Lazovic, B.V. Tadic, B. Stanojevic, L. Motte, Rhombohedron and plate-like hematite (α-Fe_2O_3) nanoparticles: synthesis, structure, morphology, magnetic properties and potential biomedical applications for MRI, Mater. Res. Bull. 133 (2021) 111055. https://doi.org/10.1016/j.materresbull.2020.111055.

[16] N. Sivakumar, J. Gajendiran, R. Jayavel, Microstructural, optical, electrochemical and magnetic properties of hydrothermal synthesized zincite/carbon (ZnO/C) composite, Chem. Phys. Lett. 745 (2020) 137262. https://doi.org/10.1016/j.cplett.2020.137262.

[17] L.N. Dem'yanets, V. V. Artemov, L.E. Li, Y.M. Mininzon, T.G. Uvarova, Zinc oxide hollow microstructures and nanostructures formed under hydrothermal conditions, Crystallogr. Reports. 53 (2008) 888–893. https://doi.org/10.1134/S1063774508050258.

[18] H.A. Rafaie, N.A.A.M. Nazam, N.I.T. Ramli, R. Mohamed, M.F. Kasim, Synthesis, characterization and photocatalytic activities of Al-doped ZnO for degradation of methyl orange dye under UV light irradiation, J. Aust. Ceram. Soc. 57 (2021) 479–488. https://doi.org/10.1007/s41779-020-00541-6.

[19] J. Chang, E.R. Waclawik, Facet-controlled self-assembly of ZnO nanocrystals by non-hydrolytic aminolysis and their photodegradation activities, CrystEngComm. 14 (2012) 4041–4048. https://doi.org/10.1039/C2CE25154J.

[20] N.A.F. Al-Rawashdeh, O. Allabadi, M.T. Aljarrah, Photocatalytic activity of graphene oxide/zinc oxide nanocomposites with embedded metal nanoparticles for the degradation of organic dyes, ACS Omega. 5 (2020) 28046–28055. https://doi.org/10.1021/acsomega.0c03608.

[21] E.H. Kisi, M.M. Elcombe, u parameters for the wurtzite structure of ZnS and ZnO using powder neutron diffraction, Acta Crystallogr. Sect. C. 45 (1989) 1867–1870. https://doi.org/10.1107/S0108270189004269.

[22] H. Mei, S. Zhou, M. Lu, L. Cheng, Tetrapod-like ZnO/$ZnFe_2O_4$ based heterostructure for enhanced ethanol detection, J. Alloys Compd. 840 (2020) 155583. https://doi.org/10.1016/j.jallcom.2020.155583.

[23] K.R. Park, R.N. Kim, Y. Song, J. Kwon, H. Choi, Facile Fabrication of ZnO-$ZnFe_2O_4$ Hollow Nanostructure by a One-Needle Syringe Electrospinning Method for a High-Selective H_2S Gas Sensor, Materials (Basel). 15 (2022) 399. https://doi.org/10.3390/ma15020399.

[24] A. Kmita, A. Pribulova, M. Holtzer, P. Futas, A. Roczniak, Use of Specific Properties of Zinc Ferrite in Innovative Technologies, Arch. Metall. Mater. 61 (2016) 2141–2146. https://doi.org/10.1515/AMM-2016-0289.

[25] I. Hussain, S. Sahoo, M.S. Sayed, M. Ahmad, M. Sufyan Javed, C. Lamiel, Y. Li, J.J. Shim, X. Ma, K. Zhang, Hollow nano- and microstructures: Mechanism, composition, applications, and factors affecting morphology and performance, Coord. Chem. Rev. 458 (2022) 214429. https://doi.org/10.1016/J.CCR.2022.214429.

[26] X. Wang, J. Feng, Y. Bai, Q. Zhang, Y. Yin, Synthesis, Properties, and Applications of Hollow Micro-/Nanostructures, Chem. Rev. 116 (2016) 10983–11060. https://doi.org/10.110.1021/acs.chemrev.5b00731.

[27] K.H. Oh, H.J. Park, S.W. Kang, J.C. Park, K.M. Nam, Synthesis of hollow iron oxide nanospheres and their application to gas sensors, J. Nanosci. Nanotechnol. 18 (2018) 1356–1360. https://doi.org/10.1166/jnn.2018.14925.

[28] J. Yu, X. Yu, Hydrothermal synthesis and photocatalytic activity of zinc oxide hollow spheres, Environ. Sci. Technol. 42 (2008) 4902–4907. https://doi.org/10.1021/es800036n.

[29] Y. Cheng, J. Cao, Y. Li, Z. Li, H. Zhao, G. Ji, Y. Du, The Outside-In Approach to Construct Fe_3O_4 Nanocrystals/Mesoporous Carbon Hollow Spheres Core-Shell Hybrids toward Microwave Absorption, ACS Sustain. Chem. Eng. 6 (2018) 1427–1435. https://doi.org/10.1021/ACSSUSCHEMENG.7B03846.

[30] G.Q. Zhao, X. Long, J. Zou, J. Hu, F.P. Jiao, Design of hollow nanostructured photocatalysts for clean energy production, Coord. Chem. Rev. 477 (2023) 214953. https://doi.org/10.1016/J.CCR.2022.214953.

[31] S.W. Chee, Z.M. Wong, Z. Baraissov, S.F. Tan, T.L. Tan, U. Mirsaidov, Interface-mediated Kirkendall effect and nanoscale void migration in bimetallic nanoparticles during interdiffusion, Nat. Commun. 10 (2019) 1–8. https://doi.org/10.1038/s41467-019-10623-0.

[32] L. Klinger, O. Kraft, E. Rabkin, A model of Kirkendall hollowing of core-shell nanowires and nanoparticles controlled by short-circuit diffusion, Acta Mater. 83 (2015) 180–186. https://doi.org/10.1016/J.ACTAMAT.2014.09.050.

[33] W. Weng, J. Lin, Y. Du, X. Ge, X. Zhou, J. Bao, Template-free synthesis of metal oxide hollow micro-/nanospheres via Ostwald ripening for lithium-ion batteries, J. Mater. Chem. A. 6 (2018) 10168–10175. https://doi.org/10.1039/C8TA03161D.

[34] T.P. Doan-Nguyen, S. Jiang, K. Koynov, K. Landfester, D. Crespy, Ultrasmall Nanocapsules Obtained by Controlling Ostwald Ripening, Angew. Chemie Int. Ed. 60 (2021) 18094–18102. https://doi.org/10.1002/ANIE.202103444.

[35] X. Feng, Q. Jiao, H. Cui, M. Yin, Q. Li, Y. Zhao, H. Li, W. Zhou, C. Feng, One-Pot Synthesis of $NiCo_2S_4$ Hollow Spheres via Sequential Ion-Exchange as an Enhanced Oxygen Bifunctional Electrocatalyst in Alkaline Solution, ACS Appl. Mater. Interfaces. 10 (2018) 29521–29531. https://doi.org/10.1021/ACSAMI.8B08547.

[36] Z. Li, C. Li, J. Huang, W. Sun, W. Cheng, C.C. He, L. Tian, Structure engineering of amorphous P–CoS hollow electrocatalysts for promoted oxygen evolution reaction, Int. J. Hydrogen Energy. 47 (2022) 15189–15197. https://doi.org/10.1016/J.IJHYDENE.2022.03.038.

[37] B.Y. Guan, L. Yu, X. Wang, S. Song, X.W.D. Lou, Formation of Onion-Like $NiCo_2S_4$ Particles via Sequential Ion-Exchange for Hybrid Supercapacitors, Adv. Mater. 29 (2017) 1605051. https://doi.org/10.1002/ADMA.201605051.

[38] S. Xiong, H.C. Zeng, Serial Ionic Exchange for the Synthesis of Multishelled Copper Sulfide Hollow Spheres, Angew. Chemie. 124 (2012) 973–976. https://doi.org/10.1002/ANGE.201106826.

[39] Z. Zhang, Y. Tao, H. Tian, Q. Yue, S. Liu, Y. Liu, X. Li, Y. Lu, Z. Sun, E. Kraka, S. Liu, Chelation-Assisted Selective Etching Construction of Hierarchical Polyoxometalate-Based Metal-Organic Framework, Chem. Mater. 32 (2020) 5550–5557. https://doi.org/10.1021/ACS.CHEMMATER.0C00440.

[40] S.E. Skrabalak, L. Au, X. Li, Y. Xia, Facile synthesis of Ag nanocubes and Au nanocages, Nat. Protoc. 2 (2007) 2182–2190. https://doi.org/10.1038/nprot.2007.326.

[41] K. An, T. Hyeon, Synthesis and biomedical applications of hollow nanostructures, Nano Today. 4 (2009) 359–373. https://doi.org/10.1016/J.NANTOD.2009.06.013.

[42] Q. Zhang, W. Wang, J. Goebl, Y. Yin, Self-templated synthesis of hollow nanostructures, Nano Today. 4 (2009) 494–507. https://doi.org/10.1016/J.NANTOD.2009.10.008.

[43] L. Yang, B. Zhang, W. Ma, Y. Du, X. Han, P. Xu, Pearson's principle-inspired strategy for the synthesis of amorphous transition metal hydroxide hollow nanocubes for electrocatalytic oxygen evolution, Mater. Chem. Front. 2 (2018) 1523–1528. https://doi.org/10.1039/C8QM00170G.

[44] Q. Fu, X. Bao, Surface chemistry and catalysis confined under two-dimensional materials, Chem. Soc. Rev. 46 (2017) 1842–1874. https://doi.org/10.1039/C6CS00424E.

[45] C. Tan, X. Cao, X.J. Wu, Q. He, J. Yang, X. Zhang, J. Chen, W. Zhao, S. Han, G.H. Nam, M. Sindoro, H. Zhang, Recent Advances in Ultrathin Two-Dimensional Nanomaterials, Chem. Rev. 117 (2017) 6225–6331. https://doi.org/10.1021/ACS.CHEMREV.6B00558.

[46] Y. Zhou, N. López, The Role of Fe Species on NiOOH in Oxygen Evolution Reactions, ACS Catal. 10 (2020) 6254–6261. https://doi.org/10.1021/acscatal.0c00304.

[47] T.M. Suzuki, T. Nonaka, A. Suda, N. Suzuki, Y. Matsuoka, T. Arai, S. Sato, T. Morikawa, Highly crystalline β-FeOOH(Cl) nanorod catalysts doped with transition metals for efficient water oxidation, Sustain. Energy Fuels. 1 (2017) 636–643. https://doi.org/10.1039/C7SE00043J.

[48] S.H. Ye, Z.X. Shi, J.X. Feng, Y.X. Tong, G.R. Li, Activating CoOOH Porous Nanosheet Arrays by Partial Iron Substitution for Efficient Oxygen Evolution Reaction, Angew. Chemie Int. Ed. 57 (2018) 2672–2676. https://doi.org/10.1002/ANIE.201712549.

[49] N.T. Suen, S.F. Hung, Q. Quan, N. Zhang, Y.J. Xu, H.M. Chen, Electrocatalysis for the oxygen evolution reaction: recent development and future perspectives, Chem. Soc. Rev. 46 (2017) 337–365. https://doi.org/10.1039/C6CS00328A.

[50] P.P. Liu, Y.Q. Zheng, H.L. Zhu, T.T. Li, Mn_2O_3 Hollow Nanotube Arrays on Ni Foam as Efficient Supercapacitors and Electrocatalysts for Oxygen Evolution Reaction, ACS Appl. Nano Mater. 2 (2019) 744–749. https://doi.org/10.1021/ACSANM.8B01918.

[51] K. Zeng, W. Li, Y. Zhou, Z. Sun, C. Lu, J. Yan, J.H. Choi, R. Yang, Multilayer hollow $MnCo_2O_4$ microsphere with oxygen vacancies as efficient electrocatalyst for oxygen evolution reaction, Chem. Eng. J. 421 (2021) 127831. https://doi.org/10.1016/J.CEJ.2020.127831.

[52] C. Wang, L. Qi, Heterostructured Inter-Doped Ruthenium–Cobalt Oxide Hollow Nanosheet Arrays for Highly Efficient Overall Water Splitting, Angew. Chemie Int. Ed. 59 (2020) 17219–17224. https://doi.org/10.1002/ANIE.202005436.

[53] X. Kuang, R. Kuang, Y. Dong, Z. Wang, X. Sun, Y. Zhang, Q. Wei, Hollow Polyhedral Arrays Composed of a Co_3O_4 Nanocrystal Ensemble on a Honeycomb-like Carbon Hybrid for Boosting Highly Active and Stable Evolution Oxygen, Inorg. Chem. 58 (2019) 3683–3689. https://doi.org/10.1021/ACS.INORGCHEM.8B03236.

[54] J. Lee, O.K. Farha, J. Roberts, K.A. Scheidt, S.T. Nguyen, J.T. Hupp, Metal–organic framework materials as catalysts, Chem. Soc. Rev. 38 (2009) 1450–1459. https://doi.org/10.1039/B807080F.

[55] L. Chen, Q. Xu, Metal-Organic Framework Composites for Catalysis, Matter. 1 (2019) 57–89. https://doi.org/10.1016/J.MATT.2019.05.018.

[56] H. Zhao, Z.Y. Yuan, Insights into Transition Metal Phosphate Materials for Efficient Electrocatalysis, ChemCatChem. 12 (2020) 3797–3810. https://doi.org/10.1002/CCTC.202000360.

[57] F.X. Ma, H. Hu, H. Bin Wu, C.Y. Xu, Z. Xu, L. Zhen, X.W. Lou, Formation of Uniform Fe_3O_4 Hollow Spheres Organized by Ultrathin Nanosheets and Their Excellent Lithium Storage Properties, Adv. Mater. 27 (2015) 4097–4101. https://doi.org/10.1002/ADMA.201501130.

[58] Z. Liu, X.Y. Yu, U. Paik, Etching-in-a-Box: A Novel Strategy to Synthesize Unique Yolk-Shelled Fe_3O_4@Carbon with an Ultralong Cycling Life for Lithium Storage, Adv. Energy Mater. 6 (2016) 1502318. https://doi.org/10.1002/AENM.201502318.

[59] L. Zhang, H. Bin Wu, S. Madhavi, H.H. Hng, X.W. Lou, Formation of Fe_2O_3 microboxes with hierarchical shell structures from metal-organic frameworks and their lithium storage properties, J. Am. Chem. Soc. 134 (2012) 17388–17391. https://doi.org/10.1021/JA307475C.

[60] X. Wang, X.L. Wu, Y.G. Guo, Y. Zhong, X. Cao, Y. Ma, J. Yao, Synthesis and Lithium Storage Properties of Co_3O_4 Nanosheet-Assembled Multishelled Hollow Spheres, Adv. Funct. Mater. 20 (2010) 1680–1686. https://doi.org/10.1002/ADFM.200902295.

[61] J. Qi, X. Lai, J. Wang, H. Tang, H. Ren, Y. Yang, Q. Jin, L. Zhang, R. Yu, G. Ma, Z. Su, H. Zhao, D. Wang, Multi-shelled hollow micro-/nanostructures, Chem. Soc. Rev. 44 (2015) 6749–6773. https://doi.org/10.1039/C5CS00344J.

[62] M. Zhu, J. Tang, W. Wei, S. Li, Recent progress in the syntheses and applications of multishelled hollow nanostructures, Mater. Chem. Front. 4 (2020) 1105–1149. https://doi.org/10.1039/c9qm00700h.

[63] H. Qian, G. Lin, Y. Zhang, P. Gunawan, R. Xu, A new approach to synthesize uniform metal oxide hollow nanospheres via controlled precipitation, Nanotechnology. 18 (2007) 355602. https://doi.org/10.1088/0957-4484/18/35/355602.

[64] X. Lai, J. Li, B.A. Korgel, Z. Dong, Z. Li, F. Su, J. Du, D. Wang, General Synthesis and Gas-Sensing Properties of Multiple-Shell Metal Oxide Hollow Microspheres, Angew. Chemie Int. Ed. 50 (2011) 2738–2741. https://doi.org/10.1002/ANIE.201004900.

[65] S.K. Kaverlavani, S.E. Moosavifard, A. Bakouei, Designing graphene-wrapped nanoporous $CuCo_2O_4$ hollow spheres electrodes for high-performance asymmetric supercapacitors, J. Mater. Chem. A. 5 (2017) 14301–14309. https://doi.org/10.1039/C7TA03943C.

[66] B.Y. Guan, A. Kushima, L. Yu, S. Li, J. Li, X.W.D. Lou, Coordination Polymers Derived General Synthesis of Multishelled Mixed Metal-Oxide Particles for Hybrid Supercapacitors, Adv. Mater. 29 (2017) 1605902. https://doi.org/10.1002/ADMA.201605902.

[67] S. Kamari Kaverlavani, S.E. Moosavifard, A. Bakouei, Self-templated synthesis of uniform nanoporous $CuCo_2O_4$ double-shelled hollow microspheres for high-performance asymmetric supercapacitors, Chem. Commun. 53 (2017) 1052–1055. https://doi.org/10.1039/C6CC08888K.

[68] X. Xu, Z. Zhang, X. Wang, Well-Defined Metal–Organic-Framework Hollow Nanostructures for Catalytic Reactions Involving Gases, Adv. Mater. 27 (2015) 5365–5371. https://doi.org/10.1002/ADMA.201500789.

[69] H. Ren, R. Yu, J. Wang, Q. Jin, M. Yang, D. Mao, D. Kisailus, H. Zhao, D. Wang, Multishelled TiO_2 hollow microspheres as anodes with superior reversible capacity for lithium ion batteries, Nano Lett. 14 (2014) 6679–6684. https://doi.org/10.1021/NL503378A.

[70] J. Shin, R.M. Anisur, M.K. Ko, G.H. Im, J.H. Lee, I.S. Lee, Hollow Manganese Oxide Nanoparticles as Multifunctional Agents for Magnetic Resonance Imaging and Drug Delivery, Angew. Chemie Int. Ed. 48 (2009) 321–324. https://doi.org/10.1002/ANIE.200802323.

[71] S. Shi, F. Chen, W. Cai, Biomedical applications of functionalized hollow mesoporous silica nanoparticles: focusing on molecular imaging, Nanomedicine. 8 (2013) 2027–2039. https://doi.org/10.2217/NNM.13.177.

[72] L. Wang, Z. Lou, T. Fei, T. Zhang, Zinc oxide core–shell hollow microspheres with multi-shelled architecture for gas sensor applications, J. Mater. Chem. 21 (2011) 19331–19336. https://doi.org/10.1039/C1JM13354C.

[73] G. Mohammadi Ziarani, M. Malmir, N. Lashgari, A. Badiei, The role of hollow magnetic nanoparticles in drug delivery, RSC Adv. 9 (2019) 25094–25106. https://doi.org/10.1039/c9ra01589b.

[74] Y. Wang, G. Wang, H. Wang, C. Liang, W. Cai, L. Zhang, Chemical-Template Synthesis of Micro/Nanoscale Magnesium Silicate Hollow Spheres for Waste-Water Treatment, Chem. – A Eur. J. 16 (2010) 3497–3503. https://doi.org/10.1002/CHEM.200902799.

[75] H. Lim, M. Yusuf, S. Song, S. Park, K.H. Park, Efficient photocatalytic degradation of dyes using photo-deposited Ag nanoparticles on ZnO structures: simple morphological control of ZnO, RSC Adv. 11 (2021) 8709–8717. https://doi.org/10.1039/d0ra10945b.

[76] Y. Liang, N. Guo, L. Li, R. Li, G. Ji, S. Gan, Facile synthesis of Ag/ZnO micro-flowers and their improved ultraviolet and visible light photocatalytic activity, New J. Chem. 40 (2016) 1587–1594. https://doi.org/10.1039/c5nj02388b.

[77] M. Xiao, Z. Wang, M. Lyu, B. Luo, S. Wang, G. Liu, H.M. Cheng, L. Wang, Hollow Nanostructures for Photocatalysis: Advantages and Challenges, Adv. Mater. 31 (2019) 1801369. https://doi.org/10.1002/ADMA.201801369.

[78] S. Gu, Y. Chen, R. Hao, J. Zhou, I. Hussain, N. Qin, M. Li, J. Chen, Z. Wang, W. Zheng, Q. Gan, Z. Li, H. Guo, Y. Li, K. Zhang, Z. Lu, Redox of naphthalenediimide radicals in a 3D polyimide for stable Li-ion batteries, Chem. Commun. 57 (2021) 7810–7813. https://doi.org/10.1039/D1CC02426D.

[79] Z. Wang, L. Zhou, X.W. Lou, Metal Oxide Hollow Nanostructures for Lithium-ion Batteries, Adv. Mater. 24 (2012) 1903–1911. https://doi.org/10.1002/ADMA.201200469.

[80] C. Xu, Y. Jiang, J. Yang, W. Wu, X. Qian, L. Hou, Co-Fe-MoS_x hollow nanoboxes as high-performance counter electrode catalysts for Pt-free dye-sensitized solar cells, Chem. Eng. J. 343 (2018) 86–94. https://doi.org/10.1016/J.CEJ.2018.02.121.

[81] W.J. Youngblood, S.H. Anna Lee, K. Maeda, T.E. Mallouk, Visible light water splitting using dye-sensitized oxide semiconductors, Acc. Chem. Res. 42 (2009) 1966–1973. https://doi.org/10.1021/AR9002398.

[82] Q. Wang, H. Zhao, F. Li, W. She, X. Wang, L. Xu, H. Jiao, Mo-doped Ni_2P hollow nanostructures: highly efficient and durable bifunctional electrocatalysts for alkaline water splitting, J. Mater. Chem. A. 7 (2019) 7636–7643. https://doi.org/10.1039/C9TA01015G.

[83] G. Wang, X. Zhou, J. Qin, Y. Liang, B. Feng, Y. Deng, Y. Zhao, J. Wei, General Synthesis of Mixed Semiconducting Metal Oxide Hollow Spheres with Tunable Compositions for Low-Temperature Chemiresistive Sensing, ACS Appl. Mater. Interfaces. 11 (2019) 35060–35067. https://doi.org/10.1021/ACSAMI.9B08694.

[84] S. Nozohouri, R. Salehi, S. Ghanbarzadeh, K. Adibkia, H. Hamishehkar, A multilayer hollow nanocarrier for pulmonary co-drug delivery of methotrexate and doxorubicin in the form of dry powder inhalation formulation, Mater. Sci. Eng. C. 99 (2019) 752–761. https://doi.org/10.1016/J.MSEC.2019.02.009.

[85] D.D. Vuong, L.H. Phuoc, V.X. Hien, N.D. Chien, Hydrothermal synthesis and ethanol-sensing properties of α-Fe_2O_3 hollow nanospindles, Mater. Sci. Semicond. Process. 107 (2020) 104861. https://doi.org/10.1016/j.mssp.2019.104861.

[86] X. Qiao, J. Huang, Nanoneedle-assembled hollow α-Fe_2O_3 microflowers as Li-ion battery anode with high capacity and good temperature tolerance, J. Electroanal. Chem. 898 (2021) 115625. https://doi.org/10.1016/j.jelechem.2021.115625.

[87] H. Yin, Y.L. Zhao, Q. Hua, J. Zhang, Y. Zhang, X. Xu, Y. Long, J. Tang, F. Wang, Controlled synthesis of hollow α-Fe_2O_3 microspheres assembled with ionic liquid for enhanced visible-light photocatalytic activity, Front. Chem. 7 (2019) 58. https://doi.org/10.3389/fchem.2019.00058.

[88] M. Qiu, R. Wang, X. Qi, Hollow polyhedral α-Fe_2O_3 prepared by self-assembly and its photocatalytic activities in degradation of RhB, J. Taiwan Inst. Chem. Eng. 102 (2019) 394–402. https://doi.org/10.1016/j.jtice.2019.05.024.

[89] L. Song, G. Wang, X. Su, J. Hu, Y. Cao, Facile synthesis of hollow α-Fe_2O_3 nanospindle and its superior photocatalytic performance for water oxidation, Catal. Commun. 154 (2021) 106306. https://doi.org/10.1016/j.catcom.2021.106306.

[90] H. Song, T. Chen, X. Zhang, X. Jia, One-step template-free synthesis of hollow core-shell α-Fe_2O_3 microspheres with improved lithium storage and gas-sensing properties, CrystEngComm. 17 (2015) 1173–1181. https://doi.org/10.1039/C4CE01996B.

[91] N.M. Abdul Rashid, C. Haw, W. Chiu, N.H. Khanis, A. Rohaizad, P. Khiew, S. Abdul Rahman, Structural- and optical-properties analysis of single crystalline hematite (α-Fe_2O_3) nanocubes prepared by one-pot hydrothermal approach, CrystEngComm. 18 (2016) 4720–4732. https://doi.org/10.1039/C6CE00573J.

[92] G. Binitha, M.S. Soumya, A.A. Madhavan, P. Praveen, A. Balakrishnan, K.R.V. Subramanian, M. V. Reddy, S. V. Nair, A.S. Nair, N. Sivakumar, Electrospun α-Fe_2O_3 nanostructures for supercapacitor applications, J. Mater. Chem. A. 1 (2013) 11698–11704. https://doi.org/10.1039/c3ta12352a.

[93] X. Qi, H. Zhang, Z. Zhang, Y. Bian, A. Shen, P. Xu, Y. Zhao, Subunits controlled synthesis of three-dimensional hierarchical flower-like α-Fe_2O_3 hollow spheres as high-performance anodes for lithium ion batteries, Appl. Surf. Sci. 452 (2018) 174–180. https://doi.org/10.1016/j.apsusc.2018.04.253.

[94] Q. Gao, J. Luo, X. Wang, C. Gao, M. Ge, Novel hollow α-Fe_2O_3 nanofibers via electrospinning for dye adsorption, Nanoscale Res. Lett. 10 (2015) 176. https://doi.org/10.1186/s11671-015-0874-7.

[95] W. Chen, X. Fan, M. Sun, H. Xie, The cube-shaped hematite microrobot for biomedical application, Mechatronics. 74 (2021) 102498. https://doi.org/10.1016/j.mechatronics.2021.102498.

[96] S. Demirci, M. Yurddaskal, T. Dikici, C. Sarıoğlu, Fabrication and characterization of novel iodine doped hollow and mesoporous hematite (Fe_2O_3) particles derived from sol-gel method and their photocatalytic performances, J. Hazard. Mater. 345 (2018) 27–37. https://doi.org/10.1016/j.jhazmat.2017.11.009.

[97] M. Akia, K.A. Mkhoyan, K. Lozano, Synthesis of multiwall α-Fe_2O_3 hollow fibers via a centrifugal spinning technique, Mater. Sci. Eng. C. 102 (2019) 552–557. https://doi.org/10.1016/j.msec.2019.04.085.

[98] J.W. Jung, J.S. Jang, T.G. Yun, K.R. Yoon, I.D. Kim, Three-Dimensional Nanofibrous Air Electrode Assembled With Carbon Nanotubes-Bridged Hollow Fe_2O_3 Nanoparticles for High-Performance Lithium-Oxygen Batteries, ACS Appl. Mater. Interfaces. 10 (2018) 6531–6540. https://doi.org/10.1021/acsami.7b15421.

[99] B. Wang, J.S. Chen, H. Bin Wu, B. Wu, Z. Wang, X.W. (David) Lou, Quasiemulsion-Templated Formation of α-Fe_2O_3 Hollow Spheres with Enhanced Lithium Storage Properties, J. Am. Chem. Soc. 133 (2011) 17146–17148. https://doi.org/10.1021/ja208346s.

[100] L. de los S. Valladares, L. León Félix, S.M. Espinoza Suarez, A.G. Bustamante Dominguez, T. Mitrelias, S. Holmes, N.O. Moreno, J. Albino Aguiar, C.H.W. Barnes, Preparation and crystallization of hollow α-Fe_2O_3 microspheres following the gas-bubble template method, Mater. Chem. Phys. 169 (2016) 21–27. https://doi.org/10.1016/j.matchemphys.2015.11.021.

[101] Y. Huo, Y. Zhu, J. Xie, G. Cao, T. Zhu, X. Zhao, S. Zhang, Controllable synthesis of hollow α-Fe_2O_3 nanostructures, their growth mechanism, and the morphology-reserved conversion to magnetic Fe_3O_4/C nanocomposites, RSC Adv. 3 (2013) 19097–19103. https://doi.org/10.1039/c3ra42764a.

[102] G. Li, R. Han, X. Xu, M. Ren, Facile synthesis of Mn-doped hollow Fe_2O_3 nanospheres coated with polypyrrole as anodes for high-performance lithium-ion batteries, RSC Adv. 6 (2016) 48199–48204. https://doi.org/10.1039/C6RA08740J.

[103] L. Dang, H. Ma, J. Xu, Y. Jin, J. Wang, Q. Lu, F. Gao, Hollow α-Fe_2O_3 core-shell colloidosomes: Facile one-pot synthesis and high lithium anodic performances, CrystEngComm. 18 (2016) 544–549. https://doi.org/10.1039/C5CE02037A.

[104] T. Ma, L. Zheng, Y. Zhao, Y. Xu, J. Zhang, X. Liu, Highly porous double-shelled hollow hematite nanoparticles for gas sensing, ACS Appl. Nano Mater. 2 (2019) 2347–2357. https://doi.org/10.1021/acsanm.9b00228.

[105] G. Niraula, J.A.H. Coaquira, G. Zoppellaro, B.M.G. Villar, F. Garcia, A.F. Bakuzis, J.P.F. Longo, M.C. Rodrigues, D. Muraca, A.I. Ayesh, F.S.M. Sinfrônio, A.S. De Menezes, G.F. Goya, S.K. Sharma, Engineering Shape Anisotropy of Fe_3O_4-γ-Fe_2O_3 Hollow Nanoparticles for Magnetic Hyperthermia, ACS Appl. Nano Mater. 4 (2021) 3148–3158. https://doi.org/10.1021/acsanm.1c00311.

[106] H.M. Abdelaal, A. Tawfik, A. Shaikjee, A simple approach to synthesis uniform 3D hollow yttrium oxide spheres using a hydrothermal scheme, Mater. Chem. Phys. 242 (2020) 122530. https://doi.org/10.1016/j.matchemphys.2019.122530.

[107] X. Ding, J. Jin, X. Huang, S. Zhou, A. Xiao, Y. Chen, C. Zuo, An in situ template for the synthesis of tunable hollow carbon particles for high-performance lithium-sulfur batteries, ACS Omega. 4 (2019) 16088–16094. https://doi.org/10.1021/acsomega.9b02287.

[108] M. Wang, H.P. Hu, Q.Y. Chen, G.F. Ji, FT-IR, XPS, and DFT study of adsorption mechanism of sodium acetohydroxamate onto goethite or hematite, Chin. J. Chem. Phys. 29 (2016) 308–318. https://doi.org/10.1063/1674-0068/29/cjcp1508182.

[109] M. Qayoom, K.A. Shah, A.H. Pandit, A. Firdous, G.N. Dar, Dielectric and electrical studies on iron oxide (α-Fe_2O_3) nanoparticles synthesized by modified solution combustion reaction for microwave applications, J. Electroceram. 45 (2020) 7–14. https://doi.org/10.1007/s10832-020-00219-2.

[110] X.Q. Chen, S. Bin Wu, R.B. Cao, J.S. Tao, Preparation and characterization of nanosized hematite colloids using green vitriol as ferrum source, J. Nanomater. 2014 (2014) 749562. https://doi.org/10.1155/2014/749562.

[111] V. V. Atuchin, D.A. Vinnik, T.A. Gavrilova, S.A. Gudkova, L.I. Isaenko, X. Jiang, L.D. Pokrovsky, I.P. Prosvirin, L.S. Mashkovtseva, Z. Lin, Flux Crystal Growth and the Electronic Structure of $BaFe_{12}O_{19}$ Hexaferrite, J. Phys. Chem. C. 120 (2016) 5114–5123. https://doi.org/10.1021/acs.jpcc.5b12243.

[112] M.I.U. Hoque, Y. Yamauchi, R. Naidu, R. Holze, R. Saidur, Q. Qu, M.M. Rahman, N.L. Torad, M.S.A. Hossain, M. Kim, J. Kim, S.H.A. Ahmad, A.U. Rehman, M.S.H. Firoz, U. Luba, S. Chowdhury, A.N. Chowdhury, A facile synthesis of hematite nanorods from rice starch and their application to Pb(II) ions removal, ChemistrySelect. 4 (2019) 3730–3736. https://doi.org/10.1002/slct.201802462.

[113] D. Trpkov, M. Panjan, L. Kopanja, M. Tadić, Hydrothermal synthesis, morphology, magnetic properties and self-assembly of hierarchical α-Fe_2O_3 (hematite) mushroom-, cube- and sphere-like superstructures, Appl. Surf. Sci. 457 (2018) 427–438. https://doi.org/10.1016/j.apsusc.2018.06.224.

[114] M. Thommes, K. Kaneko, A. V. Neimark, J.P. Olivier, F. Rodriguez-Reinoso, J. Rouquerol, K.S.W. Sing, Physisorption of gases, with special reference to the evaluation of surface area and pore size distribution (IUPAC Technical Report), Pure Appl. Chem. 87 (2015) 1051–1069. https://doi.org/10.1515/pac-2014-1117.

[115] A. Mukhtar, N. Mellon, S. Saqib, S.P. Lee, M.A. Bustam, Extension of BET theory to CO_2 adsorption isotherms for ultra-microporosity of covalent organic polymers, SN Appl. Sci. 2 (2020) 1232. https://doi.org/10.1007/s42452-020-2968-9.

[116] Y. Noh, T. Umeda, Y. Musha, K. Itatani, Fabrication of novel bone haemostasis sheet by using sugar-containing hydroxyapatite and plant-derived polymer, R. Soc. Open Sci. 6 (2019) 181649. https://doi.org/10.1098/rsos.181649.

[117] A.G. Bannov, M. V. Popov, P.B. Kurmashov, Thermal analysis of carbon nanomaterials: advantages and problems of interpretation, J. Therm. Anal. Calorim. 142 (2020) 349–370. https://doi.org/10.1007/s10973-020-09647-2.

[118] E. Darezereshki, F. Bakhtiari, M. Alizadeh, A. Behrad Vakylabad, M. Ranjbar, Direct thermal decomposition synthesis and characterization of hematite (α-Fe_2O_3) nanoparticles, Mater. Sci. Semicond. Process. 15 (2012) 91–97. https://doi.org/10.1016/j.mssp.2011.09.009.

[119] B. Janani, A. Syed, A.M. Thomas, S. Al-Rashed, A.M. Elgorban, L.L. Raju, S.S. Khan, A simple approach for the synthesis of bi-functional p-n type ZnO@$CuFe_2O_4$ heterojunction nanocomposite for photocatalytic and antimicrobial application, Phys. E Low-Dimensional Syst. Nanostructures. 130 (2021) 114664. https://doi.org/10.1016/j.physe.2021.114664.

[120] V. Anh Tran, T. Khoa Phung, V. Thuan Le, T. Ky Vo, T. Tai Nguyen, T. Anh Nga Nguyen, D. Quoc Viet, V. Quang Hieu, T.T. Thi Vo, Solar-light-driven photocatalytic degradation of methyl orange dye over Co_3O_4-ZnO nanoparticles, Mater. Lett. 284 (2021) 128902. https://doi.org/10.1016/j.matlet.2020.128902.

[121] A. Haghighatzadeh, B. Mazinani, M. Ostad, M. Shokouhimehr, J. Dutta, Hollow ZnO microspheres self-assembled from rod-like nanostructures: morphology-dependent linear and Kerr-type nonlinear optical properties, J. Mater. Sci. Mater. Electron. 32 (2021) 23385–23398. https://doi.org/10.1007/s10854-021-06827-0.

[122] S. Parvaz, M. Rabbani, R. Rahimi, Fabrication of novel magnetic ZnO hollow spheres/pumice nanocomposites for photodegradation of Rhodamine B under visible light irradiation, Mater. Sci. Eng. B Solid-State Mater. Adv. Technol. 263 (2021) 114863. https://doi.org/10.1016/j.mseb.2020.114863.

[123] L. Zhao, F. Dai, D. Fan, Y. Chen, C. Zheng, Z. Yang, Z. Zhuang, K. Pi, J. Mo, J. Deng, Synthesis and optical properties of solid and hollow ZnO microspheres prepared by hydrothermal method, Medziagotyra. 24 (2018) 367–371. https://doi.org/10.5755/j01.ms.24.4.19141.

[124] G. Song, W. Li, Fabrication of hollow ZnO particles and its photocatalytic property by modifying of nano ZnS, J. Nanosci. Nanotechnol. 13 (2013) 1364–1367. https://doi.org/10.1166/jnn.2013.6030.

[125] Y. Bao, L. Gao, C. Feng, J. Ma, W. Zhang, C. Liu, D. Simion, Hollow flower-like ZnO: Synthesis, growth mechanism and application in polyacrylate, Adv. Powder Technol. 31 (2020) 1975–1984. https://doi.org/10.1016/j.apt.2020.02.030.

[126] W. Zhang, K. Strobl, Hollow ZnO nano-cone synthesis via catalyst free MOCVD, MRS Online Proc. Libr. 1350 (2011) 942. https://doi.org/10.1557/opl.2011.1328.

[127] G.-R. Cho, D.-H. Kim, D.-H. Lee, A facile approach to fabrication of hollow ZnO nanoparticles, Compos. Res. 31 (2018) 94–98. https://doi.org/10.7234/composres.2018.31.3.094.

[128] J. Cheng, X. Yang, H. Tian, B. Zhao, D. Zhang, Catalyst-free synthesis of hollow-sphere-like ZnO and its photoluminescence property, Adv. Mater. Sci. Eng. 2014 (2014) 567278. https://doi.org/10.1155/2014/567278.

[129] Y. Yan, Q. Liu, J. Wang, L. Ji, X. Jing, R. Li, L. Liu, Synthesis of ZnO hollow microspheres via an in-situ gas growth method, Powder Technol. 232 (2012) 134–140. https://doi.org/10.1016/j.powtec.2012.08.010.

[130] K.J. Ju, M. Zhang, Q.L. Zhang, J. Wei, A.J. Wang, Facile synthesis of rambutan-like ZnO hierarchical hollow microspheres with highly photocatalytic activity, J. Nanomater. 2015 (2015) 242798. https://doi.org/10.1155/2015/242798.

[131] M. Yin, S. Liu, Preparation of ZnO hollow spheres with different surface roughness and their enhanced gas sensing property, Sensors Actuators, B Chem. 197 (2014) 58–65. https://doi.org/10.1016/j.snb.2014.02.071.

[132] J. Liu, Y. Zhao, J. Ma, Y. Dai, J. Li, J. Zhang, Flower-like ZnO hollow microspheres on ceramic mesh substrate for photocatalytic reduction of Cr(VI) in tannery wastewater, Ceram. Int. 42 (2016) 15968–15974. https://doi.org/10.1016/j.ceramint.2016.07.098.

[133] L. Li, L. Han, Y. Han, Z. Yang, B. Su, Z. Lei, Preparation and enhanced photocatalytic properties of 3D nanoarchitectural ZnO hollow spheres with porous shells, Nanomaterials. 8 (2018) 687. https://doi.org/10.3390/nano8090687.

[134] X. Wang, M. Liao, Y. Zhong, J.Y. Zheng, W. Tian, T. Zhai, C. Zhi, Y. Ma, J. Yao, Y. Bando, D. Golberg, ZnO hollow spheres with double-yolk egg structure for high-performance photocatalysts and photodetectors, Adv. Mater. 24 (2012) 3421–3425. https://doi.org/10.1002/adma.201201139.

[135] L. Xue, A. Zhang, J. Wu, Q. Wang, Y. Liu, Y. Zhao, S. Liu, Z. Liu, P. Li, S. Zeng, Surface modification and reconstruction of ZnO hollow microspheres for selective electroreduction of CO_2 to CO, J. Alloys Compd. 882 (2021) 160703. https://doi.org/10.1016/j.jallcom.2021.160703.

[136] L.H. Minh, P.T. Thuy Thu, B.Q. Thanh, N.T. Hanh, D.T. Thu Hanh, N. Van Toan, C.M. Hung, N. Van Duy, P. Van Tong, N.D. Hoa, Hollow ZnO nanorices prepared by a simple hydrothermal method for NO_2 and SO_2 gas sensors, RSC Adv. 11 (2021) 33613–33625. https://doi.org/10.1039/d1ra05912b.

[137] L. Yu, W. Hao, Z. Li, X. Ren, H. Yang, H. Ma, Synthesis of ZnO core/shell hollow microspheres to boost light harvesting capability in quantum dots-sensitized solar cell, Chem. Phys. Lett. 764 (2021) 138283. https://doi.org/10.1016/j.cplett.2020.138283.

[138] S. Jeyabharathi, R. Mahalakshmi, S. Chandramohan, S. Naveenkumar, K. Sundar, A. Muthukumaran, Self-assembled hollow ZnO nano and micro donut shape by starch and its antimicrobial potentials, Mater. Lett. 275 (2020) 128128. https://doi.org/10.1016/j.matlet.2020.128128.

[139] P. Prasongsook, V. Lachom, N. Kenyota, P. Laokul, Characterization and photocatalytic performance of hollow zinc oxide microspheres prepared via a template-free hydrothermal method, Mater. Chem. Phys. 237 (2019) 121836. https://doi.org/10.1016/j.matchemphys.2019.121836.

[140] S. Salem, M. Sakir, K. Sahin, I. Korkmaz, E. Yavuz, G. Sarp, M.S. Onses, E. Yilmaz, Low bandgap microsphere-like magnetic nanocomposite: an enhanced photocatalyst for degradation of organic contaminants and fabrication of SERS-active surfaces, Colloids Surfaces A Physicochem. Eng. Asp. 589 (2020) 124436. https://doi.org/10.1016/j.colsurfa.2020.124436.

[141] S.M. Lam, Z.H. Jaffari, J.C. Sin, H. Zeng, H. Lin, H. Li, A.R. Mohamed, D.Q. Ng, Surface decorated coral-like magnetic $BiFeO_3$ with Au nanoparticles for effective sunlight photodegradation of 2,4-D and E. coli inactivation, J. Mol. Liq. 326 (2021) 115372. https://doi.org/10.1016/j.molliq.2021.115372.

[142] Z.J. Yu, M.R. Kumar, D.L. Sun, L.T. Wang, R.Y. Hong, Large scale production of hexagonal ZnO nanoparticles using PVP as a surfactant, Mater. Lett. 166 (2016) 284–287. https://doi.org/10.1016/j.matlet.2015.12.102.

[143] U. Holzwarth, N. Gibson, The Scherrer equation versus the "Debye-Scherrer equation," Nat. Nanotechnol. 6 (2011) 534. https://doi.org/10.1038/nnano.2011.145.

[144] H. Wu, Z. Yuan, F. Nie, J. He, X. Wang, Z. Ye, Annealing temperature-dependent morphology and structure of ZnO nanoflowers for high-sensitivity ultraviolet photodetectors, J. Mater. Sci. Mater. Electron. 32 (2021) 26520–26528. https://doi.org/10.1007/s10854-021-07028-5.

[145] M. Adeel, M. Saeed, I. Khan, M. Muneer, N. Akram, Synthesis and characterization of Co-ZnO and evaluation of its photocatalytic activity for photodegradation of methyl orange, ACS Omega. 6 (2021) 1426–1435. https://doi.org/10.1021/acsomega.0c05092.

[146] H. Sun, L. Wang, D. Chu, Z. Ma, A. Wang, Y. Zheng, L. Wang, Facile template-free hydrothermal fabrication of ZnO hollow microspheres for gas sensing applications, Ceram. Int. 40 (2014) 16465–16473. https://doi.org/10.1016/j.ceramint.2014.07.156.

[147] J. Jiang, G. Wang, Y. Shao, J. Wang, S. Zhou, Y. Su, Step-scheme ZnO@ZnS hollow microspheres for improved photocatalytic H_2 production performance, Chinese J. Catal. 43 (2022) 329–338. https://doi.org/10.1016/S1872-2067(21)63889-5

[148] J.C. Sin, J. Quek, S.M. Lam, H. Zeng, H. Lin, H. Li, K.O. Tham, A.R. Mohamed, J.W. Lim, Punica granatum mediated green synthesis of cauliflower-like ZnO and decorated with bovine bone-derived hydroxyapatite for expeditious visible light photocatalytic antibacterial, antibiofilm and antioxidant activities, J. Environ. Chem. Eng. 9 (2021) 105736. https://doi.org/10.1016/j.jece.2021.105736.

[149] Sunaina, S. Devi, S.T. Nishanthi, S.K. Mehta, A.K. Ganguli, M. Jha, Surface photosensitization of ZnO by ZnS to enhance the photodegradation efficiency for organic pollutants, SN Appl. Sci. 3 (2021) 689. https://doi.org/10.1007/s42452-021-04643-z.

[150] H.Y. Phin, J.C. Sin, S.H. Tan, T.L. Chew, Y.T. Ong, Fabrication of asymmetric zinc oxide/carbon nanotubes coated polysulfone photocatalytic nanocomposite membrane for fouling mitigation, J. Appl. Polym. Sci. 138 (2021). https://doi.org/10.1002/app.51194.

[151] J. Estrada-Urbina, A. Cruz-Alonso, M. Santander-González, A. Méndez-Albores, A. Vázquez-Durán, Nanoscale zinc oxide particles for improving the physiological and sanitary quality of a mexican landrace of red maize, Nanomaterials. 8 (2018) 1–12. https://doi.org/10.3390/nano8040247.

[152] T.N. Ravishankar, M.D.O. Vaz, S.R. Teixeira, The effects of surfactant in the sol-gel synthesis of CuO/TiO_2 nanocomposites on its photocatalytic activities under UV-visible and visible light illuminations, New J. Chem. 44 (2020) 1888–1904. https://doi.org/10.1039/c9nj05246a.

[153] A. Šarić, M. Vrankić, D. Lützenkirchen-Hecht, I. Despotović, Ž. Petrović, G. Dražić, F. Eckelt, Insight into the Growth Mechanism and Photocatalytic Behavior of Tubular Hierarchical ZnO Structures: An Integrated Experimental and Theoretical Approach, Inorg. Chem. (2022). https://doi.org/10.1021/acs.inorgchem.1c03905.

[154] E. Kowsari, Sonochemically assisted synthesis and application of hollow spheres, hollow prism, and coralline-like ZnO nanophotocatalyst, J. Nanoparticle Res. 13 (2011) 3363–3376. https://doi.org/10.1007/s11051-011-0255-9.

[155] S. Duo, R. Zhong, Z. Liu, J. Wang, T. Liu, C. Huang, H. Wu, One-step hydrothermal synthesis of ZnO microflowers and their composition-/hollow nanorod-dependent wettability and photocatalytic property, J. Phys. Chem. Solids. 120 (2018) 20–33. https://doi.org/10.1016/j.jpcs.2018.04.019.

[156] K. Rambabu, G. Bharath, F. Banat, P.L. Show, Green synthesis of zinc oxide nanoparticles using Phoenix dactylifera waste as bioreductant for effective dye degradation and antibacterial performance in wastewater treatment, J. Hazard. Mater. 402 (2021) 123560. https://doi.org/10.1016/j.jhazmat.2020.123560.

[157] H.R. Khan, G. Murtaza, M.A. Choudhary, Z. Ahmed, M.A. Malik, Photocatalytic removal of carcinogenic reactive red S3B dye by using ZnO and Cu doped ZnO nanoparticles synthesized by polyol method: A kinetic study, Sol. Energy. 173 (2018) 875–881. https://doi.org/10.1016/j.solener.2018.08.038.

[158] S. Chakraborty, J.J. Farida, R. Simon, S. Kasthuri, N.L. Mary, Averrhoe carrambola fruit extract assisted green synthesis of zno nanoparticles for the photodegradation of congo red dye, Surfaces and Interfaces. 19 (2020) 100488. https://doi.org/10.1016/j.surfin.2020.100488.

[159] P. Pascariu, C. Cojocaru, N. Olaru, P. Samoila, A. Airinei, M. Ignat, L. Sacarescu, D. Timpu, Novel rare earth (RE-La, Er, Sm) metal doped ZnO photocatalysts for degradation of Congo-Red dye: Synthesis, characterization and kinetic studies, J. Environ. Manage. 239 (2019) 225–234. https://doi.org/10.1016/j.jenvman.2019.03.060.

[160] U. Sirimahachai, S. Phongpaichit, S. Wongnawa, Evaluation of bactericidal activity of TiO_2 photocatalysts: a comparative study of laboratory-made and commercial TiO_2 samples, Songklanakarin J. Sci. Technol. 31 (2009) 517–525.

[161] S.M. Lam, J.C. Sin, H. Lin, H. Li, H. Zeng, Greywater and bacteria removal with synchronized energy production in photocatalytic fuel cell based on anodic TiO_2/ZnO/Zn and cathodic CuO/Cu, Chemosphere. 245 (2020) 125565. https://doi.org/10.1016/j.chemosphere.2019.125565.

[162] T. Sansenya, N. Masri, T. Chankhanittha, T. Senasu, J. Piriyanon, S. Mukdasai, S. Nanan, Hydrothermal synthesis of ZnO photocatalyst for detoxification of anionic azo dyes and antibiotic, J. Phys. Chem. Solids. 160 (2022) 110353. https://doi.org/10.1016/j.jpcs.2021.110353.

[163] Y.H. Chin, J.C. Sin, S.M. Lam, H. Zeng, H. Lin, H. Li, A.R. Mohamed, 0-D/3-D heterojunction composite constructed by decorating transition metal oxide nanoparticle on peony-like ZnO hierarchical microstructure for improved photodegradation of palm oil mill effluent, Optik (Stuttg). 260 (2022) 169098. https://doi.org/10.1016/j.ijleo.2022.169098.

[164] S. Selvinsimpson, P. Gnanamozhi, V. Pandiyan, M. Govindasamy, M.A. Habila, N. Al Masoud, Y. Chen, Synergetic effect of Sn doped ZnO nanoparticles synthesized via ultrasonication technique and its photocatalytic and antibacterial activity, Environ. Res. 197 (2021) 111115. https://doi.org/10.1016/j.envres.2021.111115.

[165] R.K. Sharma, Ankita, R. Singh, A. Kumar, N. Goyal, A time saving ZnO nanoparticle fabrication approach for bulk photocatalytic applications, Mater. Today Proc. 45 (2021) 4906–4909. https://doi.org/10.1016/j.matpr.2021.01.360.

[166] J. Li, Z. Liu, Z. Zhu, Magnetically separable $ZnFe_2O_4$, $Fe_2O_3/ZnFe_2O_4$ and $ZnO/ZnFe_2O_4$ hollow nanospheres with enhanced visible photocatalytic properties, RSC Adv. 4 (2014) 51302–51308. https://doi.org/10.1039/c4ra06389a.

[167] J. Li, X. Lai, C. Xing, D. Wang, One-pot synthesis of porous hematite hollow microspheres and their application in water treatment, J. Nanosci. Nanotechnol. 10 (2010) 7707–7710. https://doi.org/10.1166/jnn.2010.2795.

[168] L. Hou, L. Lian, L. Zhang, G. Pang, C. Yuan, Self-Sacrifice Template Fabrication of Hierarchical Mesoporous Bi-Component-Active $ZnO/ZnFe_2O_4$ Sub-Microcubes as Superior Anode Towards High-Performance Lithium-Ion Battery, Adv. Funct. Mater. 25 (2015) 238–246. https://doi.org/10.1002/adfm.201402827.

[169] S. Wang, X. Gao, J. Yang, Z. Zhu, H. Zhang, Y. Wang, Synthesis and gas sensor application of $ZnFe_2O_4$-ZnO composite hollow microspheres, RSC Adv. 4 (2014) 57967–57974. https://doi.org/10.1039/C4RA10659H.

[170] X. Ma, X. Zhou, Y. Gong, N. Han, H. Liu, Y. Chen, MOF-derived hierarchical $ZnO/ZnFe_2O_4$ hollow cubes for enhanced acetone gas-sensing performance, RSC Adv. 7 (2017) 34609–34617. https://doi.org/10.1039/c7ra04437b.

[171] R. Zhang, T. Zhang, T. Zhou, Z. Lou, J. Deng, L. Wang, Fast and real-time acetone gas sensor using hybrid $ZnFe_2O_4$/ZnO hollow spheres, RSC Adv. 6 (2016) 66738–66744. https://doi.org/10.1039/c6ra12201a.

[172] S.D. Kulkarni, S. Kumbar, S.G. Menon, K.S. Choudhari, C. Santhosh, Magnetically separable core-shell $ZnFe_2O_4$@ZnO nanoparticles for visible light photodegradation of methyl orange, Mater. Res. Bull. 77 (2016) 70–77. https://doi.org/10.1016/j.materresbull.2016.01.022.

[173] L. Sun, R. Shao, L. Tang, Z. Chen, Synthesis of $ZnFe_2O_4$/ZnO nanocomposites immobilized on graphene with enhanced photocatalytic activity under solar light irradiation, J. Alloys Compd. 564 (2013) 55–62. https://doi.org/10.1016/j.jallcom.2013.02.147.

[174] R. Shao, L. Sun, L. Tang, Zhidong Chen, Preparation and characterization of magnetic core-shell $ZnFe_2O_4$@ZnO nanoparticles and their application for the photodegradation of methylene blue, Chem. Eng. J. 217 (2013) 185–191. https://doi.org/10.1016/j.cej.2012.11.109.

[175] M. Zhao, J. Huang, Y. Zhou, X. Pan, H. He, Z. Ye, X. Pan, Controlled synthesis of spinel $ZnFe_2O_4$ decorated ZnO heterostructures as peroxidase mimetics for enhanced colorimetric biosensing, Chem. Commun. 49 (2013) 7656–7658. https://doi.org/10.1039/c3cc43154a.

[176] Y. Li, G. Dai, C. Zhou, Q. Zhang, Q. Wan, L. Fu, J. Zhang, R. Liu, C. Cao, A. Pan, Y. Zhang, B. Zou, Formation and optical properties of ZnO:$ZnFe_2O_4$ superlattice microwires, Nano Res. 3 (2010) 326–338. https://doi.org/10.1007/s12274-010-1036-y.

[177] J. Liu, M. Zeng, R. Yu, Surfactant-free synthesis of octahedral ZnO/$ZnFe_2O_4$ heterostructure with ultrahigh and selective adsorption capacity of malachite green, Sci. Rep. 6 (2016) 1–10. https://doi.org/10.1038/srep25074.

[178] H. Liu, C. Han, C. Shao, S. Yang, X. Li, B. Li, X. Li, J. Ma, Y. Liu, ZnO/$ZnFe_2O_4$ Janus Hollow Nanofibers with Magnetic Separability for Photocatalytic Degradation of Water-Soluble Organic Dyes, ACS Appl. Nano Mater. 2 (2019) 4879–4890. https://doi.org/10.1021/acsanm.9b00838.

[179] X. Li, C. Wang, H. Guo, P. Sun, F. Liu, X. Liang, G. Lu, Double-Shell Architectures of $ZnFe_2O_4$ Nanosheets on ZnO Hollow Spheres for High-Performance Gas Sensors, ACS Appl. Mater. Interfaces. 7 (2015) 17811–17818. https://doi.org/10.1021/acsami.5b04118.

[180] D.D. Qin, C.L. Tao, A nanostructured ZnO-$ZnFe_2O_4$ heterojunction for the visible light photoelectrochemical oxidation of water, RSC Adv. 4 (2014) 16968–16972. https://doi.org/10.1039/c4ra00204k.

[181] Z. Kovács, V. Márta, T. Gyulavári, Á. Ágoston, L. Baia, Z. Pap, K. Hernadi, Noble metal modified (002)-oriented ZnO hollow spheres for the degradation of a broad range of pollutants, J. Environ. Chem. Eng. 10 (2022) 107655. https://doi.org/10.1016/J.JECE.2022.107655.

[182] J. Luo, Z. Yan, R. Liu, J. Xu, X. Wang, Synthesis and excellent visible light photocatalysis performance of magnetic reduced graphene oxide/ZnO/$ZnFe_2O_4$ composites, RSC Adv. 7 (2017) 23246–23254. https://doi.org/10.1039/C7RA02083J.

[183] J. Feng, Y. Wang, L. Zou, B. Li, X. He, Y. Ren, Y. Lv, Z. Fan, Synthesis of magnetic ZnO/$ZnFe_2O_4$ by a microwave combustion method, and its high rate of adsorption of methylene blue, J. Colloid Interface Sci. 438 (2015) 318–322. https://doi.org/10.1016/j.jcis.2014.10.009.

[184] J. Wang, J. Wan, D. Wang, Hollow Multishelled Structures for Promising Applications: Understanding the Structure-Performance Correlation, Acc. Chem. Res. 52 (2019) 2169–2178. https://doi.org/10.1021/ACS.ACCOUNTS.9B00112.

[185] L. Liu, Z. Jiang, L. Fang, H. Xu, H. Zhang, X. Gu, Y. Wang, Probing the Crystal Plane Effect of Co_3O_4 for Enhanced Electrocatalytic Performance toward Efficient Overall Water Splitting, ACS Appl. Mater. Interfaces. 9 (2017) 27736–27744. https://doi.org/10.1021/ACSAMI.7B07793.

List of publications

1. Sucrose-derived carbon template-assisted synthesis of zinc oxide hollow microspheres: Investigating the effect of hollow morphology on photocatalytic activity

   Md Shahadat Hossain, Takeshi Furusawa, Masahide Sato

   Inorganic Chemistry Communications, 148 (2023), 110376

2. Hydrothermal synthesis, characterization and thermal stability studies of α-Fe_2O_3 hollow microspheres

   Md Shahadat Hossain, Takeshi Furusawa, Masahide Sato

   Advanced Powder Technology, 33 (2022), 103797

List of presentations

1. **Md Shahadat Hossain**, Takeshi Furusawa, Masahide Sato, Fabrication of hollow ZnO-$ZnFe_2O_4$ composite microspheres by a sucrose-based hydrothermal technique. The 73rd Divisional Meeting of Division of Colloid and Surface Chemistry, Hiroshima University, Hiroshima, Japan. September 20-22, 2022.

2. **Md Shahadat Hossain**, Takeshi Furusawa, Masahide Sato, Facile synthesis of hollow α-Fe2O3 microspheres by hydrothermal method. The 72nd Divisional Meeting of Division of Colloid and Surface Chemistry, Utsunomiya University, Utsunomiya, Japan. September 15-18, 2021.